Heterogeneous and specific localization of mRNAs at dendritic spine and its dependence on microtubule entry and kinesin motor

Xiaojie Wang[1], Jiaxing Song[1], Jiahao Lin[1], Tian Tian[2], Alex Tsun-Lok Lui[1], Bryan Cheuk-Yu Lee[1], Liang Zhang[2,3], and Kwok-On Lai[1,3#]

[1]Department of Neuroscience, 2Department of Biomedical Sciences,
[3]Hong Kong Institute for Advanced Study, City University of Hong Kong

*Equal contributions of the authors
#To whom correspondence should be addressed:
Prof. Kwok-On Lai
Department of Neuroscience, City University of Hong Kong
Phone: 852-3442-4152
E-mail: kwokolai@cityu.edu.hk

Running title: heterogeneous synaptic localization of mRNAs

ABSTRACT

Local mRNA translation near neuronal synapses is believed to underlie changes in connectivity during long-term synaptic plasticity and memory formation, yet how the mRNAs localize at synapses is not well-studied. In particular, whether different dendritic mRNAs might display differential synaptic localization via interaction with specific proteins remains unexplored. Here we found that two well-known dendritic mRNAs, *Actb* and *Camk2a* are targeted to different subdomains of dendritic spines and delivered to different spine populations in response to chemical long-term potentiation (cLTP). Surprisingly, the induced mRNA localization to dendritic spines is associated with microtubule entry and depends on the kinesin motor protein KIF5A. Proximity-labelling proteomic further identifies distinct postsynaptic proteins enriched by the two mRNAs, with selected candidates showing mRNA co-localization at dendritic spines. Our study provides new insights on the heterogeneous localization of mRNAs at the synapses and demonstrates proximity-labelling as a useful approach to identify their synaptic partners that might contribute to their differential distribution.

INTRODUCTION

Neurons extend dendritic arbors spanning hundreds of micrometers from the soma, creating a spatial constraint that demands precise protein localization. Rather than relying solely on translation in the soma and subsequent transport of the proteins, neurons synthesize a subset of proteins locally near synapses, which enables rapid changes of protein composition in response to synaptic activity. This local translation is fundamental to consolidating long-term synaptic plasticity and memory (Holt and Schuman, 2013; Buxbaum et al. 2014; Cajigas et al., 2012; Steward and Schuman, 2001). The soma-to-dendrite long-range transport of mRNAs requires the formation of ribonucleoprotein granules via specific RNA-binding proteins (RBPs), which are then carried by the kinesin motor proteins along microtubules (Kiebler and Bassell, 2006; Mitsumori et al., 2017; Kanai et al., 2004). To achieve synapse-specific plasticity, mRNA translation can occur within a single dendritic spine, thereby selectively modulating the protein composition of the activated postsynaptic sites (Doyle and Kiebler, 2011). Indeed, the heads and base of dendritic spines, which are the compartments where excitatory synapses are located, can capture mRNAs from the dendritic shaft, especially after synaptic stimulation. Chemical long-term potentiation (cLTP) increases the abundance of mRNAs like *Camk2a*, *Actb*, and *Psd95* near dendritic spines (Donlin-Asp et al., 2021). Stimulation by two-photon glutamate uncaging also recruits *Rgs4* and *Actb* mRNA granules to the activated spines, indicating synapse-specific targeting (Yoon et al., 2016; Bauer et al., 2019).

Compared to the microtubule-mediated long-range transport, much less is known about the short-range delivery and subsequent localization of mRNAs to dendritic spines. The actin/myosin motor system is regarded as the major short-range transport system in neurons (Hammer III and Sellers, 2011), but recent work demonstrates the entry of microtubule and its associated proteins to dendritic spines upon synaptic stimulation (Jaworski et al., 2009; Hu et al., 2011), raising the possibility that kinesin could also contribute to the synaptic targeting of mRNAs. Instead of being transported together as single entities, individual mRNAs are transported from soma to the dendrite as separate ribonucleoprotein granules (Tübing et al., 2010; Mikl et al., 2011; Batish et al., 2012). These granules contain diverse compositions of both mRNAs and proteins (Fritzsche et al., 2013; Mitsumori et al., 2017). Recent multiplexed *in situ* hybridization also reveals that thousands of dendritic mRNAs are heterogeneously distributed along dendrite (Wang et al., 2020). However, the key question of whether these initially separate granules end up to the same or different dendritic spines as destination in response to stimulation remains unexplored. Given that individual synapses of the same neurons can have diverse protein compositions (Grant and Fransen, 2020; Oostrum and Schuman, 2024) and different proteins can be distributed at specific subdomains within a single spine, it is conceivable that

mRNAs might undergo similar diversity in their synaptic localization. There is also little information about how specific mRNAs ultimately localize differentially at dendritic compartments. Are there specific RBPs and motor proteins responsible for bringing different mRNAs to the synapses? Do mRNAs localize at dendritic spines through interaction with specific synaptic proteins?

To begin addressing these questions, we focus on the *Actb* and *Camk2a* mRNAs—two well-characterized dendritically localized mRNAs and their encoded proteins have established functions in synaptic plasticity. Through single-molecule fluorescence *in situ* hybridization (smFISH) and proximity labelling proteomics, we characterize the heterogeneity and specificity of the activity-dependent mRNA localization. We further reveal the role of microtubule and kinesin motors in mediating their synaptic localization, as well as identify through proximity-labeling proteomics the putative synaptic proteins that colocalize with these mRNAs at dendritic spine. These findings suggest a multi-step mechanism in achieving synapse-specific mRNA localization, which may represent a post-transcriptional regulatory mechanism that fine-tunes the composition of individual dendritic spines in response to synaptic stimulation.

RESULTS

Differential localization of *Actb* and *Camk2a* mRNAs at specific subdomains of dendritic spines

Both the base and the head of dendritic spines have been reported to contain mRNAs (Tiruchinapalli et al., 2003; Kao et al., 2010; Dynes and Steward, 2012). To ask whether two different mRNAs show preference to be localized at different subdomains of dendritic spines, we visualize *Actb* and *Camk2a* mRNA simultaneously in rat hippocampal neuron and compare the distribution of the two mRNA at dendritic compartments within the same neurons. A sense probe was used as a negative control to rule out any non-specific signal. Specificity of two antisense probes were validated through exogenous expression of the transcripts in HEK 293T cells (Fig. S1). We classify the mRNA distribution into three different dendritic domains: the dendritic shaft, underneath the dendritic spine (spine base), and within the head of dendritic spine (spine head) (Fig 1A). Both mRNAs were more frequently detected at the base than the head of dendritic spines, but *Actb* exhibited a higher percentage of localization at the spine heads compared to *Camk2a* in the same dendrites (Fig 1B). Consistent with previous studies (Mikl et al., 2011; Batish et al., 2012), there was little co-localization between the two mRNAs on the dendrites. Interestingly, the colocalization was significantly higher at the base of dendritic spines (Fig 1C-D). In contrast, the two mRNAs rarely colocalized within the same dendritic spine head. This finding suggests that although the two mRNAs are initially transported to the dendrites as separate granules, they are commonly destined to the base of dendritic spine which serves as the hot spot for mRNA localization. To verify this notion, we visualized *Actb* mRNA movement using the MS2 system followed by time-lapse imaging (one frame per 10 seconds for 30 minutes). Neurons were co-transfected with the MS2 mRNA reporter and GFP-MCP construct with Td-tomato to label the dendritic spines. Compared to the granules on the dendritic shaft, *Actb* mRNAs showed reduced movement of at the base of dendritic spines (Fig 1E-F). Notably, the *Actb* mRNA granules were observed to selectively stop underneath dendritic spines (Fig 1G). Quantification revealed that more than 40% of the moving *Actb* mRNAs demonstrated selective docking at the spine base (Fig 1H). These findings confirm the base of dendritic spines plays a crucial role for mRNA localization.

Next, we investigate the possibility of differential localization of *Actb* and *Camk2a* mRNAs after synaptic stimulation. cLTP is a widely used experimental paradigm to induce activity-dependent plasticity at glutamatergic synapses of cultured hippocampal neurons. Medium containing the NMDA receptor co-agonist glycine was applied to rat hippocampal neurons to induce cLTP. Thirty minutes after the brief glycine stimulation, there was a significant increase in dendritic spine size (Fig 2A-B),

particularly the mushroom spines (representing mature spines), which was accompanied with a reduction in the density of the immature filopodia (Fig. S2A-B). The change in spine morphology therefore validates the effectiveness of the stimulation paradigm. After cLTP, the colocalization of *Actb* and *Camk2a* at the spine base was significantly decreased (Fig 2C), suggesting that the two different mRNA granules become separated and targeted to different destinations. Notably, the differential distribution of *Actb* and *Camk2a* at the subdomains of dendritic spines becomes more apparent after cLTP, with *Actb* showing increasing localization at the spine heads over time, while *Camk2a* concurrently accumulating at the spine base (Fig. 2D). To confirm the increased *Actb* mRNA localization at the spine head after cLTP, we performed live-cell imaging to compare the localization of the MS2-*Actb* reporter under different conditions. Approximately 9% of the *Actb* reporter mRNA granules were localized at the spine head at the first timeframe after cLTP induction, while none of the puncta localized at the spine head under the control treatment (Fig. S2C-D). mRNA granules at the base of dendritic spines were relatively stationary under both conditions (Fig. S2E), while *Actb* reporter granules located at the spine head also showed significantly less movement compared to those at the dendritic shaft (Fig. S2F). Our findings therefore reveal that although there is increased localization of both *Actb* and *Camk2a* mRNAs towards dendritic spines after synaptic stimulation, the two different mRNAs display heterogeneous localization at different subdomains of dendritic spines within the same neurons.

Actb and *Camk2a* mRNAs are targeted to different populations of dendritic spines after cLTP

To achieve local translation, mRNAs are packaged into granules and are transported along microtubules within the dendrite (Das et al., 2021). MAP2, a microtubule-stabilizing protein, participates in activity-dependent synaptic plasticity, and cLTP results in the invasion of MAP2 from the dendritic shaft to the heads of dendritic spines (Kim et al., 2020). Consistent with this study, we found that stimulation of neurons by cLTP resulted in the presence of MAP2 in dendritic spines after 30 mins (Fig. 2E). Increasing the duration of glycine stimulation (from 3 to 6 minutes) significantly enhanced the proportion of neurons that exhibit MAP2 signals in the spine heads (Fig. S3A). The MAP2 entry to spine was completely abolished by the NMDA receptor antagonist APV, indicating glycine-induced cLTP is dependent upon NMDA receptor activation (Fig. 2E, Fig. S3B). For those neurons that showed MAP2 immunoreactivity in the spine heads after cLTP, only about half of their spines demonstrated MAP2 invasion (Fig. S3C), and these MAP2-positive spines were significantly larger than the other spines that were devoid of MAP2 fluorescence (refer as MAP2-negative spines) (Fig. 2F). Notably, the MAP2-positive spines were more likely to capture *Actb* and *Camk2a* mRNAs than the MAP2-negative spines within the same neurons (Fig. 2G-H). After cLTP induction, there was

also a parallel increase between the entry of MAP2 to the spine heads and localization of the two mRNAs at dendritic spines over time (Fig. 2I-J). Next, we investigate whether *Actb* and *Camk2a* mRNAs show differential targeting to the two populations (MAP2-positive versus MAP2-negative) of dendritic spines. Towards this end, we focus on the mRNAs within the spine head. Intriguingly, *Actb* and *Camk2a* display differential preferences towards the two populations of spines: *Camk2a* mRNAs in the spine heads were almost exclusively (99%) found in the MAP2-positive spines, whereas considerable proportion (~36%) of *Actb* mRNA were localized to the heads of MAP2-negative spines (Fig. 3A-B).

Dendritic spines may also be classified based on their enrichment of specific organelles. For example, stacks of smooth endoplasmic reticulum form a distinctive organelle called the spine apparatus, which is present in subsets of dendritic spines (Konietzny et al., 2023). The spine apparatus is typically located near the spine neck and is believed to regulate calcium homeostasis and protein synthesis within dendritic spines (Falahati et al., 2025; Konietzny et al., 2023; Pierce et al., 2000, 2001; Segal et al., 2010). The actin-binding protein Synaptopodin (SP) is commonly used as the marker for the spine apparatus (Vlachos, 2012). By transfecting hippocampal neurons with BFP and GFP-SP (Fig. S4A), we found that almost half of the dendritic spines were enriched with GFP-SP (51.75% ± 0.85%, n = 30, refer as SP-enriched spines), suggesting the presence of spine apparatus in these spines. The SP-enriched spines were more likely to contain the ribosomal protein L4 (Fig. 3C), particularly in the MAP2-positive spines (Fig. 3D-E). smFISH further revealed that, similar to the MAP2-positive spines, the SP-enriched spines were more likely to contain mRNA granules at their base and head than those without SP enrichment (Fig. 3F). These findings prompt us to explore whether *Actb* and *Camk2a* mRNAs also exhibit differential targeting to the SP-enriched spines. Indeed, compared to *Actb*, *Camk2a* displayed a higher preference to the SP-enriched spines, a trend that became more pronounced after cLTP (Fig 3G-H). Together with the selective preference to the MAP2-positive spines (Fig. 3A-B) and different subdomains of dendritic spines (Fig. 2D), our findings provide compelling evidence that the targeting of *Actb* and *Camk2a* mRNAs to dendritic spines after synaptic stimulation is heterogeneous and highly specific.

Microtubules are involved in delivering mRNAs to dendritic spines upon synaptic stimulation

Next, we investigate the mechanism by which cLTP induces *Actb* and *Camk2a* mRNAs to dendritic spines. Since dendritic spines that contain MAP2 after synaptic stimulation are more likely to capture mRNAs (Fig. 2H), we reason that microtubule entry plays a crucial role in delivering the two mRNAs to the dendritic spines. To test this hypothesis, we first examine microtubule invasion to

dendritic spine by performing a time-course analysis following cLTP on the localization of MAP2 and EB3, a microtubule plus-end binding protein. We observed a distinct temporal pattern, in which EB3 presence in the spine head peaked as early as 5 minutes post-stimulation and subsequently declined, whereas MAP2 accumulation in spines increased progressively over time (Fig. 4A-B). This dynamic is consistent with their respective functions: EB3 marks actively polymerizing microtubule ends that spearheads the initial invasion, while MAP2 subsequently stabilizes the newly formed microtubule tracks. Importantly, EB3 granules were specifically enriched in MAP2-positive spines following cLTP (Fig. 4C), demonstrating a strong correlation between dynamic microtubule entry and the formation of a stable, MAP2-rich spine compartment that would be crucial for the subsequent recruitment of mRNAs to these spines.

To test the causal role of microtubule invasion in mRNA targeting to dendritic spine, LifeAct-MTED, which couples the Microtubule Elimination Domain (MTED) to the actin-binding peptide LifeAct, was expressed in hippocampal neurons to specifically disrupt microtubule invasion into dendritic spine (Fig. 4D). This tool leverages the high actin concentration in spines to locally eliminate microtubules, thereby inhibiting their invasion without altering overall microtubule dynamics in the dendritic shaft or general neuronal health (Holland et al., 2024). The spine density was relatively unaffected by LifeAct-MTED expression (Fig. S5A). As expected, cLTP triggered a significant increase in EB3 density in the control neurons that expressed the LifeAct-scramble control (Fig. S5B). However, expression of LifeAct-MTED profoundly suppressed the influx of both the dynamic microtubule tip protein EB3 and the stabilizing protein MAP2 into spines across all time points after cLTP (Fig. 4E, Fig. S5C), confirming that the localization of both EB3 and MAP2 to spines is strictly dependent on microtubule entry. Most importantly, the blockade of microtubule invasion significantly reduced the localization of *Actb* and *Camk2a* mRNAs to the spine heads and spine base, respectively, after cLTP (Fig. 4F). These findings provide direct evidence that microtubule entry into spines is a prerequisite for the activity-dependent synaptic targeting of *Actb* and *Camk2a* mRNAs.

Transport of *Actb* and *Camk2a* mRNAs to dendritic spine specifically requires the kinesin motor protein KIF5A but not the closely related KIF5B

Kinesin motor moves towards the plus end of microtubule to mediate anterograde transport in axons and dendrites (Hirokawa and Takemura, 2004; Hirokawa and Tanaka, 2015). The kinesin-1 family, which consists of three homologous members KIF5A, KIF5B and KIF5C, are the major molecular motors associated with mRNA transport in the mouse brain. Given their non-overlapping functions in dendritic spine morphogenesis (Zhao et al., 2020), it is possible that different mRNAs utilize different motor proteins for trafficking. To investigate whether the microtubule-dependent

mRNA delivery to dendritic spines is mediated by specific kinesin motors, we focus on the neuron-specific kinesin-1 motor KIF5A. Knockdown of KIF5A specifically reduced the density of *Camk2a* mRNA in apical dendrites, while the *Actb* mRNA density was unaffected (Fig. 5A-B). The somatic fluorescence intensity of *Camk2a,* but not *Actb* mRNA, also decreased upon KIF5A knockdown (Fig. 5C). Nonetheless, the proximo-distal distribution of *Camk2a* mRNA puncta along apical dendrites was reduced upon KIF5A knockdown (Fig. S5D), confirming that the transport of *Camk2a* mRNA depends on KIF5A. KIF5A knockdown completely abolished the cLTP-induced dendritic spine localization of *Camk2a* as well as *Actb*, as the increase in *Actb* mRNA in the spine heads and *Camk2a* mRNA at the spine bases was both eliminated by the KIF5A-shRNA. Notably, the localization of both mRNAs at dendritic spine could only be rescued by the co-expression of RNAi-resistant KIF5A (KIF5Air) but not KIF5B (KIF5Bir) (Fig. 5D-E), suggesting that the two similar kinesin motors do not share redundant functions in the synaptic delivery of the mRNAs and KIF5A is specifically required for this process. Neither the spine density, mRNA abundance nor the cLTP-induced spine enlargement was altered by the knockdown of KIF5A (Fig. S5E-G), indicating that the impaired mRNA localization at dendritic spine is not due to reduced spine number nor lack of response to the cLTP stimulation. These findings therefore identify KIF5A as the crucial and specific motor that mediates the cLTP-induced and microtubule-based transport of mRNAs to dendritic spines. Importantly, the observation that KIF5A depletion specifically interferes with the cLTP-induced *Actb* localization at dendritic spine without disrupting its overall transport to the dendrites indicates that the two types of mRNA transport (long-range soma-to-dendrite and the short-range delivery to dendritic spine) can be independently carried out by different motor proteins.

The C-terminals of KIF5A (residues 808–1027) and KIF5B (residues 808–963) contain the cargo-binding domain and the diverse carboxyl-tail that determines the functional specificity of the two kinesins in dendritic spine morphogenesis of hippocampal neurons (Zhao et al., 2020). We therefore hypothesize that the C-terminal domains of the three KIF5 heavy chains might associate with distinct RBPs that could contribute to specificity in RNA transport. To test this hypothesis, we perform APEX2-mediated proximity labelling to identify putative proteins that selectively interact with different KIF5 motors. Fusion proteins comprising the C-terminal regions of KIF5A, KIF5B, and KIF5C with APEX2 were constructed and electroporated into primary cortical neurons, with the plasmid containing only the APEX2 backbone as the negative control (Fig. 6A-C). Biotinylated proteins were enriched by streptavidin beads and identified by mass spectrometry. Three biological replicates were included for each experimental condition, and the subsequent PCA plot showing strong consistency among the triplicates (Fig. 6D). 500 proteins were identified to be enriched with statistical significance in the KIF5-APEX2 proteome relative to the APEX2 control (Fig. 6E). Many of these

KIF5-proximity proteins are also present in the postsynaptic density proteome (Kaizuka et al., 2024). In addition, several RBPs reported to be localized in dendrite were enriched by all three KIF5s, including KHDRBS1 (also known as SAM68). On the other hand, there are dendritic RBPs that show selective enrichments by specific KIF5 motors. For example, CAPRIN1 and YBX1 were enriched only by KIF5B and KIF5C, whereas FMRP was enriched selectively by KIF5A (Fig. 6F-G). These findings suggest that the three different KIF5 motors could indeed be responsible for the heterogeneous transport of various mRNAs through coupling to different RBPs.

***Actb* and *Camk2a* mRNAs are localized in proximity to different synaptic proteins in neurons**

To directly address whether there are specific proteins that localize *Actb* and *Camk2a* mRNAs to the dendritic spines, we attempt to identify the differential interactomes of the two mRNAs via CARPID, an CRISPR-based RNA-centric proximity labelling strategy that biotin-label proteins located within ~20 nm to the RNA of interest in their native cellular context (Yi et al., 2020). Towards this end, cortical neurons were transfected with two constructs, one expressing the dCas13x.1 fused with the biotin-ligase BASU, and the other expressing a set of three gRNAs targeting either *Actb* or *Camk2a* mRNA, respectively (Fig. 7A-B). A scrambled gRNA was used as the negative control in parallel. The electroporation efficiency of CARPID plasmids was verified by immunostaining (Fig. S6A). Each experimental condition contained biological triplicates which showed strong consistency, as indicated by the PCA plot (Fig. S6B). The patterns of enriched proteins in the two mRNA clusters exhibit clear differences (Fig. 7C-D). Of the 521 proteins enriched by *Camk2a* mRNA, 361 proteins were enriched only in the *Camk2a* but not *Actb* cluster; wherease among the 464 total enriched by *Actb* mRNA, 304 proteins were enriched specifically in the *Actb* mRNA cluster. There were 160 overlapping proteins being identified in both mRNA clusters (Fig. 7E). Of note, ZBP1 (IGF2BP1) and Sam68 (KHDBS1) which are known RBPs of *Actb* mRNA were identified in the *Actb* mRNA cluster, thereby validating the CARPID method in isolating RNA-interacting proteins from the neurons. We then compared our data to the published proteome datasets of meta-analyses encompassing a total of 5,869 postsynaptic protein (Kaizuka et al., 2024). Among the PSD proteins present in the datasets, 82 were specifically enriched in the *Camk2a* mRNA cluster and 77 were enriched in the *Actb* one (Fig. 7F). GO analysis revealed that the two clusters of proteins are involved in different biological processes and cellular compartments. (Fig. 7G). Remarkably, when we specifically examine the GO categories that include the term “postsynaptic”, these GO terms only came up in the *Camk2a*-proximity proteome (Fig. 8A).

To validate the CARPID data, we selected ZBP1 and Septin7 for immunostaining and dual-color smFISH to examine their co-localization with *Actb* and *Camk2a* at different subdomains of dendritic spines in hippocampal neurons (Fig. 8B). Co-localization of the mRNAs with the selected proteins

were observed on dendrites, hence confirming the CARPID proximity labeling results. Although ZBP-1 was specifically enriched in the *Actb-proximity* proteome, its co-localization between *Actb* and *Camk2a* was similar and most of the co-localized puncta were present on the dendritic shaft instead of underneath or inside the dendritic spines (Fig. 8C). In contrast, majority of the mRNA co-localization with Septin7, a protein localized mainly at the spine base and is crucial for dendritic spine growth and remodeling (Xie et al., 2007), were detected at the spine base, and this specific localization is especially pronounced for *Camk2a*. Our findings show that the CARPID proximity labelling is a useful tool to identify putative proteins that interact with *Actb* and *Camk2a* mRNAs at different subcellular compartments of neurons, including different subdomains of dendritic spines such as the spine neck and postsynaptic density.

DISCUSSION

While the transport of mRNAs along dendrites is well-documented, whether different transcripts are differentially targeted and distributed within individual dendritic spines remains poorly understood. In this study, we reveal a high degree of spatial heterogeneity in the sub-spine localization of two dendritic mRNAs, *Actb* and *Camk2a,* which are essential for synaptic plasticity. Although both mRNAs accumulate at the base of dendritic spines, which might act as a potential "reservoir" of mRNAs for subsequent translation, cLTP induces the specific localization of *Actb* mRNA in the spine head, whereas *Camk2a* mRNA preferentially anchors at the spine base. Our findings further indicate the invasion of microtubules and MAP2 as the prerequisite "gating" mechanism for this activity-dependent mRNA recruitment that also depends on the microtubule-based kinesin motor KIF5A. Finally, CARPID proximity-labeling proteomics identify the distinct protein interactomes of these mRNAs, including proteins present at the synapses. Collectively, our findings propose a multi-step model where cytoskeletal dynamics and interactions with specific proteins orchestrate the precise sub-compartmentalization of mRNAs to support synapse-specific plasticity.

The Spine Base as a Strategic Reservoir

Based on the increased co-localization of *Actb* and *Camk2a* mRNAs at the spine base, we suggest this dendritic subdomain as the primary docking site for the precise sub-synaptic organization that mirrors the localization of *Arc* (Dynes & Steward, 2012). We propose that the spine base may function as a strategic "hot spot," potentially optimizing the trade-off between proximity and spatial constraints. Structurally, the spine head is a highly restricted compartment with densely packed scaffold proteins and receptors in the PSD (Swulius et al., 2010). Anchoring mRNAs at the spine base, which is enriched with translation machinery and polyribosomes, likely allows neurons to maintain a pool of "poised" transcripts close enough to the synapses but without overcrowding the spine head, which serves the important function of neurotransmission. In addition, we postulate that this mRNA reservoir at the spine base provides functional flexibility. Instead of being “locked” within the head of a particular spine, localization at the base facilitates the redistribution of mRNAs to neighboring synapses if local activity does not reach the threshold for plasticity. Live-cell imaging indicates that *Actb* granules that dock underneath dendritic spines are still dynamic and can soon move away from the initial anchoring spines, hence supporting the notion that docking at the spine base serves as a checkpoint rather than a terminal destination. Upon synaptic stimulation by cLTP, the reservoir underneath the spine base might become mobilized, and the subsequent translocation to the spine head conceivably ensures that the synthesis of β-actin is spatially confined to the active spine, providing the structural substrate required for spine enlargement while minimizing ectopic effect at non-stimulated

sites (Yoon et al., 2016).

Activity-Dependent Sorting into Distinct Spine Subdomains and Populations

Our study reveals that cLTP induction leads to divergence in the spatial organization of *Actb* and *Camk2a* mRNAs. We postulate that this spatial segregation likely reflects the distinct properties and functional demands of their encoded proteins during plasticity. β-actin is the primary building block for spine enlargement. Upon polymerization into F-actin, the large size of the polymer makes it difficult to translocate elsewhere. Therefore, the specific localization of *Actb* mRNAs within the spine head is critical to concentrate the synthesis of structural components directly at the site of remodeling (Nakahata & Yasuda, 2018; Yoon et al., 2016). In contrast, the retention of *Camk2a* mRNA at the spine base might fulfil a different regulatory logic. Because of its small size and diffusible nature, CaMKIIα locally synthesized at the spine base would readily move into the spine head. Given the abundance of CaMKIIα in the PSD, it is conceivable that *Camk2a* mRNA translation needs to be highly effective. As such, it might be desirable to synthesize CaMKIIα at the spine base where polyribosomes are likely to be more abundant compared to the spine head.

Furthermore, we observed heterogeneity in their targeting to different spine populations. *Camk2a* mRNA exhibits a higher degree of selectivity with strong preference to the MAP2-positive and SP-enriched spines. In support of the latter, we found from our CARPID data the *Camk2a*-proximity proteins show larger overlap with the spine apparatus proteome (12 out of 140 spine apparatus proteins from Falahati et al., 2022) than the *Actb*-proximity ones (only 2 out of 140). These findings suggest that specific transcripts such as *Camk2a* are localized in proximity to the spine apparatus. MAP2 invasion is a hallmark of structural plasticity, often marking spines that have been functionally potentiated (Kim et al., 2020); whereas SP is a key component of the spine apparatus, an organelle associated with internal calcium stores and local protein synthesis machinery (Konietzny et al., 2023; Pierce et al., 2000; Vlachos et al., 2012). This specific accumulation suggests that *Camk2a* mRNA is not randomly distributed; instead, it is targeted based on the "calcium-handling" capacity of the spine. Since CaMKIIα is a calcium/calmodulin-dependent kinase, positioning its mRNA in SP-enriched spines could be advantageous as the translated product is spatially juxtaposed with internal calcium release sites and potentially facilitating rapid local activation. Conversely, *Actb* mRNA displays a broader distribution, localizing to both MAP2-positive and MAP2-negative spines. This observation implies that while *Camk2a* translation might be prioritized in the more mature or potentiated spines equipped with the spine apparatus, the requirement for actin remodeling is likely more universal since those dendritic spines that have not yet undergone extensive maturation marked by MAP2/SP accumulation still require continuous actin turnover to maintain their shape or undergo structural changes. Thus, the differential targeting of these two mRNAs might underscore a

sophisticated routing mechanism where transcripts are delivered to specific sub-populations of spines based on their local demands.

The CARPID proximity labeling uncovers distinct sets of proteins in the PSD proteome database that are enriched by the two mRNAs in neurons, thereby providing additional evidence that supports the heterogeneous distribution of mRNAs within specific subdomains of dendritic spine. One of the intriguing findings is that many GO terms related to postsynaptic membrane and postsynaptic density are only detected in the *Camk2a*-enriched proteins. This suggests that for those *Camk2a* mRNAs located within the spine head, they might be locally synthesized in proximity (probably ~10-20 nm) to the PSD and synaptic membrane. This would have functional relevance since many PSD proteins are substrates of CaMKIIα. On the other hand, due to the potential overcrowding problem at the PSD or near the postsynaptic membrane, *Actb* whose translation into β-actin is not necessary to be synthesized closely at those sites.

Microtubule Invasion and KIF5A-Mediated Synaptic Delivery

The actin/myosin motor system is conventionally regarded as the major short-range transport system in neurons (Hammer & Sellers, 2012). Our findings that mRNA localization at dendritic spine is impaired upon selective inhibition of microtubule polymerization at the spine head or knockdown of the kinesin motor KIF5A suggests that the actin/myosin network alone is insufficient for the synaptic recruitment of mRNAs. We demonstrate that the transient entry of EB3, which labels the dynamic microtubule, precedes the accumulation of MAP2. This could create a temporary "highway" bridging the dendritic shaft and the spine compartment (Miryala et al., 2022). This mechanism potentially explains the preferential targeting of mRNAs to the MAP2-positive spines: since these spines have successfully accommodated microtubules, they have established the necessary infrastructure for cargo delivery. From this point of view, microtubule invasion might function as a checkpoint to ensure that the energy-intensive machinery for local translation is deployed only to synapses undergoing active structural plasticity or consolidation (Holland et al., 2024).

Navigating this microtubule network requires specific motor proteins. Our investigation into the Kinesin-1 family reveals a sophisticated division of labor between long-range trafficking and local synaptic capture. For long-range transport from the soma to the dendrite, *Camk2a* and *Actb* mRNAs exhibit distinct motor dependencies. KIF5A knockdown significantly reduces the dendritic density of *Camk2a* but not *Actb*, suggesting that *Camk2a* is a specific cargo of KIF5A. This implies that neurons utilize distinct kinesin isoforms to sort mRNAs into different transport granules, potentially allowing for the differential regulation of their dendritic abundance (Swarnkar et al., 2021). However, despite the redundancy in long-range transport, where *Actb* can presumably rely on KIF5B or other kinesins

to be transported to the dendrite upon KIF5A depletion, our knockdown and rescue experiments indicate that KIF5A is indispensable and cannot be replaced by KIF5B for the cLTP-induced localization of mRNAs to the dendritic spines. The observation that KIF5A knockdown prevents *Actb* from entering the spine head, even when the transcript localization on dendrite is unaffected, demonstrates a mechanistic uncoupling between dendritic transport and synaptic delivery. We propose that KIF5A plays a specialized role in the short-range delivery, possibly by transferring RNA granules from the stable microtubules of the dendritic shaft onto the dynamic, invading microtubules in the spine. Alternatively, KIF5A may be unique among Kinesin-1 family members in its ability to navigate the steric constraints of the spine neck or interact with specific guidance factors during cLTP. This requirement, first microtubule invasion as the track followed by its stabilization by MAP2 and finally KIF5A as the motor, provides a multi-step filter to achieve the spatiotemporal control of synaptic mRNA delivery.

ACKNOWLEDGEMENTS

We are grateful to Marina Mikhaylova (The Humboldt-Universität zu Berlin) and Yi-Ping Hsueh (Academia Sinica) for the gift of the GFP-synaptopodin plasmid. We thank Angelo Flores and Yutong Wang for assisting the quantification of images, and Xuejun Li for assisting the live imaging of the MS2 reporter mRNA. This study was supported in part by the Research Grant Council of Hong Kong [Collaborative Research Fund (CRF) C1024-22G and General Research Fund (GRF) 11102422 and 11101624]; and the US National Academy of Medicine (NAM) [Healthy Longevity Catalyst Award (Hong Kong) HLCA/M-106/25].

MATERIALS AND METHODS

Table 1 Key Resources Table

Reagent type (species) or resource	Designation	Source or reference	Identifiers	Additional information
Biological sample (R. norvegicus)	Primary hippocampal neuron; primary cortical neuron	[295]	PMID, 28442576	Procedures of preparing primary neurons were described in [295]
Antibody	Rabbit polyclonal anti-tRFP (antibody against BFP)	Evogene	Cat#AB233	
Antibody	Mouse monoclonal anti-GFP (3E6)	Invitrogen	Cat#A11120	
Antibody	Chicken polyclonal anti-MAP2	Invitrogen	Cat#PA1-10005	
Antibody	Rabbit polyclonal anti-Ribosomal protein L4	Proteintech	Cat#11302-1-AP	

Antibody	Alexa 488 anti mouse IgG2a	Invitrogen	Cat#21131	
Antibody	Alexa 405 anti rabbit IgG(H+L)	Invitrogen	Cat#31556	
Antibody	Alexa 568 anti rabbit IgG(H+L)	Invitrogen	Cat#11011	
Antibody	Alexa 647 anti chicken IgG(H+L)	Invitrogen	Cat#21449	
Antibody	Alexa 405 anti chicken IgG(H+L)	Invitrogen	Cat#48260	
Antibody	mCherry-Tag Rabbit mAb	AE128	ABclonal	
Antibody	GFP Monoclonal Antibody (3E6)	A11120	Thermo Fisher	
Antibody	SEPT7 Polyclonal Antibody	13818-1-AP	Proteintech	
Antibody	MYO18A Polyclonal Antibody	14611-1-AP	Proteintech	
Antibody	14-3-3 epsilon Polyclonal Antibody	11648-2-AP	Proteintech	
Antibody	Caprin1 polyclonal antibody	15112-1-AP	Proteintech	
Antibody	MAP2 Rabbit mAb	A22206	ABclonal	
Antibody	Streptavidin-HRP	SA10001	Invitrogen	
Plasmid	HaloTag-bActinCDS-bActinUTR-MS2V5	Robert Singer	Addgene_102718	
Plasmid	pUbC-nls-ha-MCP-GFP	Robert Singer	Addgene_98916	
Plasmid	mEGFP-C1	Michael Davidson	Addgene_54759	
Plasmid	pCAG-BFP	Wilson Wong	Addgene_89685	

Plasmid	mApple-EB3-7	Michael Davidson	Addgene_54892	
Plasmid	EB3-GFP	Anna Akhmanova	Addgene_190164	
Plasmid	LifeAct-Scramble	Erik Dent	Addgene_217499	
Plasmid	LifeAct-MTED	Erik Dent	Addgene_217498	
Plasmid	GFP-synaptopodin (GFP-SP)	A kind gift from Marina Mikhaylova		
Plasmid	pSUPER-neo-GFP-scramble	pSUPER-neo-GFP-A kind gift from Othan		Constructed by inserting PCR-amplified scramble-sh 5'-TGGAAACG CCACAGAT ATC-3'sequences into the pSUPER-neo-GFP using EcoR1 and Kpn1
Plasmid	pSUPER-neo-GFP-KIF5Ash	This paper		Constructed by inserting PCR-amplified KIF5A-sh 5'-TGGAAACG CCACAGAT ATC-3'sequences

				into the pSUPER-neo-GFP using EcoR1 and Kpn1
Chemical compound	Glycine	Tocris Bioscience	Cat#0219	
Chemical compound	Strychnine	Sigma-Aldrich	Cat#S0532	
Chemical compound	Biotin	B4639	Sigma-Aldrich	
Reagents	Opti-MEM (1X)	11058-021	Gibco	
Commercial assay or kit	ViewRNA ISH Cell Assay Kit	ThermoFisher	Cat#QVC0001	
Software, algorithm	GraphPad Prism	GraphPad Prism (https,//graphpad.com)	RRID, SCR_015807	Version 9
Software, algorithm	FIJI	FIJI (https,//imagej.net/Fiji)	RRID, SCR_002285	
Software, algorithm	Nikon NIS-Elements	Nikon		Version 5.42.03
Animals	Sprague Dawley rat	Laboratory Animal Services Centre of The Chinese	N/A	

		University of Hong Kong		

Table 2 Probe Map for Camk2a transcript probe (NM_012920)

Label oligos (our ZZ oligos, bridentate gyruse transcript to our bDNA, signal is produced here) is RED and Blocker oligos (just fill in space, does not bridentate gyruse anything) is green

NM_012920 Rattus norvegicus calcium/calmodulin-dependent protein kinase IIalpha (Camk2a), mRNA. [Rattus norvegicus]

5' UTR: 1-42bp

agtcccgagcctaaagcctcgcctgcctgcccagtgccagg

Coding Sequence (CDS):42-1478bp

atggctaccatcacctgcacccgattcacggaagagtaccagctcttcgaggaactgggaaagggagccttctccgtggtgcgcaggtgtgtga
aggtgctggctggccaggagtatgctgccaagattatcaacaccaagaagctctcagccagagatcaccagaagttggaacgcgaggcccgca
tctgccgcttgttgaagcaccccaatatcgtccgactccatgacagcatctccgaggaggggcaccactaccttatcttcgatctggtcactggtgg
ggagctgttcgaagacattgtggcccgggagtattacagtgaggctgatgccagccactgtatccagcagatcctggaggctgtgctacactgtc
accagatgggggtggtgcatcgcgacctgaagcctgagaatctgttgctggcttcgaagctcaagggtgctgcggtgaagctggcagactttgg
cctggccatagaggttgagggagagcagcaggcatggtttgggttcgcagggacacctggatacctctccccagaagtgctgcggaaggaccc
atacgggaagcctgtggacctgtgggcctgtggcgtcatcctgtatatcttgctggttgggtatcccccattctgggatgaggaccagcaccgcct
gtaccagcagatcaaagctggtgcctacgatttcccatcaccagaatgggacaccgtcaccccggaagccaaggatctgatcaataagatgctga
ccatcaacccgtccaaacgcatcacggccgctgaggctctcaagcacccctggatctcgcaccgctccactgtggcctcctgcatgcacagaca
ggagaccgtggactgcctgaagaagttcaatgccaggaggaaactgaagggagccatcctcaccactatgctggccaccaggaacttctccgg
agggaagagtggaggaaacaagaagaatgatggcgtgaaggaatcctctgagagcaccaacaccaccatcgaggatgaagacaccaaagtg
cgcaaacaggaaattatcaaagtgacagagcagctgatcgaagccataagcaatggagactttgaatcctacacgaagatgtgcgaccctggaa
tgacagcctttgaaccggaggccctggggaacctggtcgagggcctggactttcatcgattctattttgaaaacctgtggtcccggaacagcaagc
ccgtgcacaccaccatcctgaaccctcacatccacctgatgggtgacgagtcagcctgcatcgcctacatccgcatcactcagtacctggatgcg
ggtggcatcccccgcacggcccagtcagaggagacccgtgtctggcaccgcagggatggaaaatggcagatcgtccacttccacagatctgg
ggcgccctccgtcctgccccattga

3' UTR:1478-1510bp

aggaccaggccagggtccctgcgctcttgctt

Table 3 Probe Map for Actb transcript probe (NM_031144)

Label oligos (our ZZ oligos, bridentate gyruse transcript to our bDNA, signal is produced here) is RED and Blocker oligos (just fill in space, does not bridentate gyruse anything) is green

NM_031144 Rattus norvegicus actin, beta (Actb), mRNA. [Rattus norvegicus] ROD

5' UTR: 1-79bp gtcgagtccgcgtccacccgcgagtacaaccttcttgcagctcctccgtcgccggtccacacccgccaccagttcgcca

Coding Sequence (CDS):79-1206bp

tggatgacgatatcgctgcgctcgtcgtcgacaacggctccggcatgtgcaaggccggcttcgcgggcgacgatgctccccgggccgtcttccc
ctccatcgtgggccgccctaggcaccagggtgtgatggtgggtatgggtcagaaggactcctacgtgggcgacgaggcccagagcaagagag
gcatcctgaccctgaagtaccccattgaacacggcattgtcaccaactgggacgatatggagaagatttggcaccacactttctacaatgagctgc
gtgtggcccctgaggagcaccctgtgctgctcaccgaggcccctctgaaccctaaggccaaccgtgaaaagatgacccagatcatgtttgagac
cttcaacaccccagccatgtacgtagccatccaggctgtgttgtccctgtatgcctctggtcgtaccactggcattgtgatggactccggagacggg
gtcacccacactgtgcccatctatgagggttacgcgctccctcatgccatcctgcgtctggacctggctggccgggacctgacagactacctcatg
aagatcctgaccgagcgtggctacagcttcaccaccacagctgagagggaaatcgtgcgtgacattaaagagaagctgtgctatgttgccctaga
cttcgagcaagagatggccactgccgcatcctcttcctccctggagaagagctatgagctgcctgacggtcaggtcatcactatcggcaatgagc
ggttccgatgccccgaggctctcttccagccttccttcctgggtatggaatcctgtggcatccatgaaactacattcaattccatcatgaagtgtgacg
ttgacatccgtaaagacctctatgccaacacagtgctgtctggtggcaccaccatgtacccaggcattgctgacaggatgcagaaggagattactg
ccctggctcctagcaccatgaagatcaagatcattgctcctcctgagcgcaagtactctgtgtggattggtggctctatcctggcctcactgtccacc
ttccagcagatgtggatcagcaagcaggagtacgatgagtccggcccctccatcgtgcaccgcaaatgcttctag

3' UTR:1206-1293bp

gcggactgttactgagctgcgttttacacccttttctttgacaaaacctaacttgcgcaaaaaaaaaaaaaaaaaaaaaaaaaaaaaaa

Animals

All experimental procedures utilized adult female Sprague Dawley rats (over 8 weeks of age), which were sourced from the Laboratory Animal Services Centre of The Chinese University of Hong Kong. The animals were housed under a standard 12-hour light/dark cycle in a temperature-controlled environment with ad libitum access to food and water. All animal handling and experimental protocols were conducted in accordance with the guidelines of the Association for Assessment and Accreditation of Laboratory Animal Care (AAALAC) and were approved by the Animal Ethics Committee of the Department of Health Technology and Consultation, Hong Kong SAR Health Department. Every effort was made to minimize suffering and discomfort throughout the study. Additionally, primary hippocampal and cortical neuronal cultures were prepared from E18-E19 embryos of both sexes.

Primary cell culture

Primary hippocampal and cortical neurons were isolated from Sprague Dawley rat embryos at embryonic day 18-19 following the methods according to our previous study (Lin et al., 2017). Hippocampal neurons were cultured at a low density of 0.4 x 10^5 cells per 18 mm coverslip in 12-well dishes for single-molecule fluorescence in situ hybridization (smFISH) and immunofluorescence staining. For live cell imaging, hippocampal neurons were cultured in 35 mm MatTek dishes (with a 14 mm central glass section, MatTek corp) coated with poly-D-lysine (1 mg/ml, Sigma P0899) at a density of 2.0 x 10^5 cells per dish in Neurobasal medium supplemented with 2% B27 and 0.5% L-glutamate.

Transfection

Transfection of hippocampal neurons with various plasmids was performed using calcium phosphate precipitation on 12-14 days *in vitro* (DIV) as described previously (Lai et al., 2008). Prior to transfection, cells were preconditioned in pre-warmed serum-free DMEM for 2 h in a 10% CO_2 incubator at 37°C. The transfection mixture was prepared by combining plasmid DNA with $CaCl_2$ solution, followed by slow addition to an equal volume of 2× HEPES buffer with gentle mixing to form precipitate. The precipitate was applied to neurons and incubated for 13 min (coverslips) or 15 min (MatTek dishes) in a 37°C, 5% CO_2 incubator. Cells were then washed twice with pre-warmed serum-free DMEM and recovered in a 10% CO_2 incubator at 37°C for 15 min, followed by incubation in original growth medium for 2 h. Finally, 0.5 mL of fresh growth medium was added to each well while 0.4 mL of original medium was replaced, bringing the total volume to approximately 1 mL per well. Transfected neurons were maintained in culture and analyzed 1-8 days post-transfection according to experimental requirements.

Chemical long-term potentiation (cLTP) induction

To induce cLTP in the primary hippocampal neuron culture, a well-established cLTP protocol was employed based on the glycine-induced LTP method described in the following paper (Kim et al., 2020). Primary hippocampal neurons were cultured on glass coverslips or MatTek dishes and maintained for 17-21 DIV under standard conditions (37 °C, 5% CO_2). To induce cLTP, coverslips were transferred into conditioned medium supplemented with 200 µM glycine and 1 µM strychnine, freshly prepared on the day of experiment. The conditioned medium consisted of spent growth medium collected prior to routine feeding-a time when endogenous glycine levels are substantially depleted—thereby ensuring effective and consistent cLTP induction. Following a 6-minute glycine exposure, coverslips were returned to their original glycine-free growth medium and allowed to recover for 5, 15, 30, 45, or 60 minutes. Neuronal responses were subsequently used for following experiments. To verify the NMDA receptor (NMDAR) dependence of cLTP, two control conditions were included: (1) cLTP + APV: cLTP induction was performed in the presence of 200 µM APV, an NMDAR antagonist; and (2) APV alone: neurons were treated with 200 µM APV without cLTP stimulation. As expected for NMDAR-dependent LTP, the cLTP-induced effects were abolished in the presence of APV.

Single-molecular Fluorescence In Situ Hybridization (smFISH)

smFISH was conducted using the ViewRNA ISH Cell Assay Kit from ThermoFisher following the manufacturer's instructions on 20-21DIV. Briefly, cells were fixed with 4% formaldehyde for 30 minutes and rinsed in 1x DEPC-PBS. Subsequently, cells were treated with detergent and then incubated with custom-designed probe sets targeting the different transcripts for 4 hours. Signal amplification was performed by sequential 30 min incubations at 40 °C with pre-amplifier, amplifier, and label probe sets. Between each hybridization and amplification step, coverslips were washed three times with wash buffer to minimize nonspecific binding. Finally, immunostaining was performed afterwards.

Live cell imaging and image analysis

The MS2 bacteriophage tagging system was used to for time-lapse live imaging to examine mRNA transport behaviours. The 3'- untranslated regions (UTRs) of mRNAs were individually subcloned into the reporter construct which contained multiple copies of RNA hairpins that bound to the phage MS2 coat protein (Yoon et al., 2016). Dissociated rat hippocampal neurons were transfected by calcium phosphate precipitation with the MS2 reporter construct for *Actb* mRNA (https://www.addgene.org/102718/) together with GFP-tagged MS2 coat protein. To visualize the

dendritic shaft and dendritic spines, the neurons were filled with red fluorescence after co-transfection with tdTomato. For effective capture of the RNA granule movement in neuronal dendrites, the Nikon Eclipse Ti2 fluorescence microscope was used, equipped with digital-zooming Nikon imaging software (NIS-Elements AR 64-bit version 5.42.03) and a sCMOS camera of 95% quantum efficiency to maximize the signal-to-noise ratio of the acquired images. A stage top incubator was used to maintain conditions of 37°C and 5% of CO_2 (TOKAI HIT USA). The light source had fast switching wavelengths for the rapid (1 second) capture of trafficking events in two different fluorescence channels. Live cell imaging was conducted at one frame per 10 seconds for 1800 seconds. Images were post-processed by clarified and denoised on the Nikon NIS-Elements software to clarify and enhance the visualization of individual puncta.

After imaging, kymographs of selected dendrites were generated in FIJI software using the 'KymoResliceWide' plugin. The kymographs were randomized and reviewed blindly, and images with low signal-to-noise ratio were excluded due to the difficulty in quantification. The tracking function in Nikon NIS-Elements software was used to track each individual mRNA granule, including their motion trajectories, heading, displacement, and total moving distance. The movement trajectory of each granule was initially tracked in every frame using the auto ROI tracking function, followed by manual frame-by-frame adjustments by the researchers.

Immunofluorescence staining, image acquisition, and quantitative analysis

Neurons were fixed in 4% paraformaldehyde/4% sucrose/PBS (pH 7.4) for 15 minutes at room temperature. To stain GFP-transfected neurons, neurons were exposed to GFP antibody (1:2000) in GDB buffer at 4 °C overnight. After triple rinsing with phosphate washing buffer (20 mM phosphate buffer and 0.5M NaCl), neurons were treated with Alexa488-conjugated anti-mouse IgG2a secondary antibody (1:2000 diluted in GDB buffer) at room temperature for 1 hour, followed by three additional washes with the phosphate washing buffer before mounting. For other immunocytochemistry experiments, cells underwent a 45-minute incubation in blocking buffer (0.4% Triton X-100 (vol/vol) and 1% BSA) at room temperature, followed by overnight incubation with primary antibodies in blocking buffer at 4 °C. Cells were washed three times with washing buffer (0.02% Triton X-100% and 1% BSA in PBS), treated with Alexa conjugate antibodies for 1 hour, followed by two washes in washing buffer and one in D-PBS before mounting with Hydromount (National Diagnosis).

Fluorescent z-stack images were captured using Nikon Ti2 confocal microscopes equipped with Nikon NIS-Elements AR 64-bit version 5.42.03. A 60x oil-immersion objective (Plan Apo 60x Oil) was utilized with the following parameters: a pinhole of 1 Airy Unit (AU), 1x optical zoom, scan speed set between 2 to 4, an interval of 0.3 μm, resolution of 2048 x 2048. Consistent acquisition settings were

maintained for images within the same experiment, with the exception of GFP or BFP staining, which facilitated the visualization of dendritic arbors and spines. Images were collected from 2 to 3 coverslips per experimental condition, and data from three independent experiments were combined for analysis. The sample size was described in figure legend.

To quantify dendritic spines in dissociated hippocampal neurons, whole neuron images were captured using a confocal microscope and then assigned random numbers. Subsequently, primary basal dendrites were chosen for analysis by a separate experimenter who was unaware of the random assignments. Dendritic spines were categorized according to predefined criteria based on a previous study (Lin et al., 2017). The length (L), head width (H), and neck width (N) of each spine were manually measured using NIS-Elements software. Mushroom spines were identified by a head width to neck width ratio (H/N) exceeding 1.5. Filopodia were characterized by a head width to neck width ratio (H/N) less than 1.2 and a length to neck width ratio (L/N) greater than 3. For each neuron, three distinct primary basal dendrites were selected and analysed to determine the average spine density.

In the analysis of smFISH images, a threshold for each specific channel was set using a negative control image. The researcher manually identified the position of puncta within the dendritic region, which was outlined based on GFP or BFP signals. During quantification, researchers opted not to perform maximal projection on z-stack images. Instead, they selected the layer with the strongest mRNA signal after smFISH to locate the mRNA, aiming to avoid counting smFISH signals from neurons that were not transfected. When analyzing the distribution of two different mRNAs on apical dendrites, selected dendrites were straightened using the 'Straighten' plugin (Kocsis et al., 1991) in FIJI. Co-localization of RBPs and mRNAs was analyzed using the GA3 (General Analysis 3) module of NIS-Elements software (version 5.42.03). RBPs and mRNAs (*Actb* and *Camk2a*) were detected using “BrightSpots2” function. The GA3 pipeline was then applied to the dendrites to analyze the co-localization of RBPs and mRNAs.

Antibodies and DNA constructs

Antibodies utilized in this study were obtained from commercial sources (Table 1). For immunofluorescence staining, Alexa-conjugated secondary antibodies (Invitrogen or Thermo Fisher) were used to specifically detect primary antibodies via fluorescence microscopy. To achieve specific knockdown of KIF5A, short hairpin RNA (shRNA) targeting KIF5A were designed. The 19-nucleotide shRNA sequences (KIF5A: 5′-TGGAAACGCCACAGATATC-3′) were derived from previously validated pSUPER-KIF5A construct. This sequence was subcloned into the pSUPER-neo-GFP vector using EcoRI and KpnI restriction sites to generate knockdown plasmids. A scrambled shRNA sequence (5′-GGCTACCTCCATTTAGTGT-3′), which lacks homology to any known human gene, was used as

a control to confirm the specificity of knockdown effects. For KIF5s-APEX2 plasmids, the HA tag-APEX2 constructs were created by cloning based on the pXR001 vector via homologous recombination. Then, the gene fragments for KIF5A (aa 808-1027), KIF5B (aa 808-963), and KIF5C (aa 808-956) were inserted before APEX2.

In vitro electroporation

Dissociated cortical cells at a density of 4×10^6 were mixed with 10 μg of plasmid in 100 μl of Opti-MEM and transferred to a cuvette (EC-002S, NEPA GENE). The cells were electroporated using Electroporator NEPA21 (Super Electroporator NEPA21 Type II, NEPA GENE) according to the manufacturer recommendations. Square electric pulses were applied at 275 V (pulse length, 0.5 ms; two pulses; interval, 50 ms; No. 2; 10 decay rate), followed by additional pulses at 20 V (pulse length, 50 ms; five pulses; interval, 50 ms; No. 5; 40 decay rate). After the electroporation, for CARPID, the cells were seeded on to 10 cm dishes at a density of 1.6×10^7 in the seeding medium for 2 h; for APEX, cells were seeded on to 6 cm dishes at a density of 4×10^6 in the seeding medium for 2 h . Then, the medium was replaced with the Growth medium, and the dishes were incubated at 37°C in a humidified 5% CO2 atmosphere for 14-16 days.

APEX2 biotin labeling

For KIF5s-APEX2, primary cortical neurons in 60 mm dishes electroporated with KIF5-APEX2 variants were replenished with 2 mL of fresh growth medium containing 500 μM biotin-phenol and incubated for 30 minutes. After incubation, 20 μL of 100 mM H_2O_2 was added to each dish to a final concentration of 1 mM H_2O_2 for 1 min. The reaction was quenched with DPBS containing 5 mM Trolox and 10 mM sodium ascorbate.

CARPID Biotin labelling

Primary neurons were cultured to DIV16, and the culture medium was replaced with fresh medium containing 200 μM biotin and incubate for 2 hours at 37°C with 5% CO2. Cells were washed with 10 ml ice-cold PBS at least three times to remove the remaining biotin followed by cell lysis with lysis buffer (50 mM Tris-HCl pH 7.4, 150 mM NaCl, 0.5% Triton X-100, 1 mM EDTA supplemented with fresh protease inhibitors) for Mass spectrometry or Western Blot.

CARPID Pull Down

Cells were washed with ice-cold PBS and lysed with lysis buffer (500 μl lysis buffer per dish) at 4 °C, then sonicated by the Bioruptor sonicator (Cycle Num:7; Time ON: 5 sec; Time OFF: 5 sec.). Then,

lysate was spun down at 15,000 r.p.m. for 15 min at 4 °C. The supernatant was quantified and normalized for protein concentration, which was sampled for input. Biotinylated proteins were enriched with MyOne T1 streptavidin beads after overnight of incubation at 4 °C with rotation, and six washes were performed with 1 ml ice-cold lysis buffer.

Immunoblotting

KIF5s-APEX2 or CARPID samples labelled by under the same conditions described above. After labelling, cells were washed twice with 1 mL of ice-cold DPBS and lysed with 500 μL of RIPA lysis buffer (50 mM Tris, 150 mM NaCl, 0.1% SDS, 0.5% sodium deoxycholate, 1% Triton X-100) supplemented with protease and phosphatase inhibitor cocktail (P1046, Beyotime). Lysates were collected by scraping, centrifuged at 13,000 ×g for 10 min, mixed with 5× loading buffer, and heated at 95 °C for 10 min. The samples were separated by SDS-PAGE and transferred to PVDF membrane. After blocking with 5% skim milk, the blots were incubated overnight at 4 °C with streptavidin-HRP or primary antibodies.

On-beads tryptic digestion and desalting

Purified biotinylated proteins bound to streptavidin-coated magnetic beads (from APEX2 or CARPID experiments) were subjected to on-bead digestion. The beads were resuspended in 80 μL of Buffer I and incubated in a thermomixer at 30 °C with agitation at 400 rpm for 60 minutes. The samples were then placed on a magnetic stand, and the supernatant was transferred to a fresh vial. To recover any remaining peptides, the beads were rinsed three times with 25 μL of Buffer II, with all light exposure minimized during this step. The wash supernatants were pooled with the initial liquid. Tryptic digestion was continued by adding an additional 500 ng of sequencing-grade trypsin to the combined supernatant and incubating the mixture overnight (~16 hours) in a thermomixer at 32 °C and 400 rpm. The digestion was quenched the following day by acidifying the solution with 10% formic acid (FA) to a final concentration of 0.4% FA.

The resulting peptides were desalted using Pierce™ C18 Tips (100 μL, Thermo Fisher Scientific) according to the manufacturer's instructions.

Liquid chromatography–mass spectrometry (LC-MS) data acquisition

LC-MS/MS analysis for the APEX2 and CARPID samples were performed on distinct platforms.

For APEX:

APEX2 peptide samples (2 μL, ~0.5 μg/μL) were injected onto a nanoflow Easy-nLC 1200 system (Thermo Fisher Scientific) coupled to a Q Exactive HF mass spectrometer (Thermo Fisher Scientific).

Peptides were separated on a reversed-phase C18 column (PepMap RSLC C18, 75 µm × 25 cm, 2 µm, 100 Å) at a constant flow rate of 250 nL/min. Separation was achieved using a 75-minute linear gradient from 7% to 25% solvent B (0.1% FA in 80% ACN) with solvent A being 0.1% FA. Data were acquired using Xcalibur software packages (v4.0.27, Thermo Fisher Scientific). The mass spectrometer was operated in data-dependent acquisition (DDA) mode. Full MS scans were acquired in the orbitrap at a resolution of 120,000 over a scan range of 350–1800 m/z, with an automatic gain control (AGC) target of 3×106. The top 12 most abundant precursor ions were selected for fragmentation using higher-energy collisional dissociation (HCD) at a normalized collision energy (NCE) of 27%. MS/MS scans were performed at a resolution of 30,000 with an AGC target of 3×105 and a dynamic exclusion window of 30 s was applied. Ions with unassigned or single charge states were excluded from MS/MS selection.

For CARPID:

The CARPID peptide samples (200 ng) were analysed using an OrbitrapTM AstralTM mass spectrometer (Thermo Scientific) connected to an Vanquish Neo system liquid chromatography (Thermo Scientific) in the data-independent acquisition (DlA) mode. Precursor ions were scanned at a mass range of 380 - 980m/z, MS1 resolution was 240000 at 200 m/z, Normalized AGC Target: 500%, Maximum IT: 5ms. 299 windows were set for DlA mode in MS2 scanning, isolation Window: 2m/z, HCD Collision Energy: 25ev, Normalized AGC Target: 500%, Maximum IT: 3ms.

MS/MS database search

Raw MS data files were processed for peptide identification and protein quantification. For the APEX2 data, Proteome Discoverer 2.2 (PD 2.2, Thermo Fisher Scientific) with the Sequest HT search engine was used. Datasets were searched against the Rattus norvegicus reference proteome from UniProt [UP000002494-10116-RAT, 47,914 entries]. The search parameters were consistent and included: trypsin as the protease, allowing up to two missed cleavages; a precursor mass tolerance of 10 ppm; and a fragment mass tolerance of 0.02 Da. Carbamidomethylation of cysteine was set as a fixed modification, while oxidation of methionine and N-terminal acetylation were set as variable modifications.

Peptide-spectrum matches (PSMs) were validated using a false discovery rate (FDR) threshold of 1% at both the peptide and protein levels. For label-free quantification (LFQ), precursor ion intensities were extracted, and protein abundances were calculated. The DIA data analysis in Spectronaut utilized a spectral library for targeted extraction, while the DDA data used the Precursor Ions Quantifier node in PD. Protein abundance was determined by summing the intensities of unique and razor peptides attributed to each protein, normalized across runs using the total peptide amount method.

For CARPID:

Raw MS-based data were acquired in DIA mode and processed using Spectronaut (version 18) by BayOmics. During the database search, trypsin was designated as the enzyme with a maximum of two missed cleavages. The search was conducted against a reviewed UniProt FASTA database for the corresponding species. In cases where hybrid-DIA mode was employed, the original data from library-building samples were included as a supplementary database. Data filtering was performed using a false discovery rate (FDR) threshold of $\leqslant$ 0.01 to generate protein identification and quantification data tables.

Statistical analysis of MS data

Normalized LFQ intensity data were log2-transformed and imported into the R environment (version 4.5.0) for statistical analysis. Missing values were imputed followed by data normalization using the quantile method. Differential expression analysis was performed using the limma package (version 3.63.13). Linear models were fitted to the data using the lmFit function, and empirical Bayes moderation was applied with the eBayes function. Proteins with an adjusted p-value (Benjamini-Hochberg FDR) of < 0.05 and an absolute log2 fold change of > 1 were considered differentially expressed.

Principal Component Analysis (PCA) and hierarchical clustering were performed using the base stats package (version 4.5.0). Gene Ontology (GO) term enrichment analysis for the differentially expressed proteins was conducted using the enrichGO function from the ClusterProfiler package (version 4.14.6). GO terms with an adjusted p-value (Benjamini-Hochberg FDR) of < 0.05 were deemed statistically significant. Data visualizations, including volcano plots, bar plots, and box plots, were generated using ggplot2 (version 3.5.1). Heatmaps were created with the pheatmap package (version 1.0.12), and Venn diagrams were generated using the VennDiagram package (version 1.7.3).

Statistical analysis

All data are presented as mean ± SEM. Normality of data distribution was assessed using the Shapiro-Wilk test. For comparisons between two groups of normally distributed data, Student's t-test was applied. Multiple group comparisons were performed using one-way ANOVA followed by Tukey's post hoc test. For experimental designs involving two independent factors, two-way ANOVA with Šídák's multiple comparisons test was used. The chi-square test was employed for categorical data analysis. In all cases, a *p*-value of less than 0.05 was considered statistically significant. All statistical

analyses were conducted using GraphPad Prism (GraphPad Software, Inc., USA).

REFERENCES

Batish, M., van den , P., Kramer, F.R., and Tyagi, S. (2012). Neuronal mRNAs travel singly into dendrites. Proceedings of the National Academy of Sciences of the United States of America *109*, 4645-4650.

Bauer, K.E., Segura, I., Gaspar, I., Scheuss, V., Illig, C., Ammer, G., Hutten, S., Basyuk, E., Fernández-Moya, S.M., Ehses, J.*, et al.* (2019). Live cell imaging reveals 3′-UTR dependent mRNA sorting to synapses. Nature Communications *10*, 3178.

Buxbaum, A. R., Wu, B., & Singer, R. H. (2014). Single β-actin mRNA detection in neurons reveals a mechanism for regulating its translatability. *Science (New York, N.Y.)*, *343*(6169), 419–422.

Buxbaum, A.R., Haimovich, G., and Singer, R.H. (2015). In the right place at the right time: visualizing and understanding mRNA localization. Nature reviews Molecular cell biology *16*, 95-109.

Cajigas, I.J., Tushev, G., Will, T.J., tom Dieck, S., Fuerst, N., and Schuman, E.M. (2012). The local transcriptome in the synaptic neuropil revealed by deep sequencing and high-resolution imaging. Neuron *74*, 453-466.

Das, S., Vera, M., Gandin, V., Singer, R.H., and Tutucci, E. (2021). Intracellular mRNA transport and localized translation. Nature Reviews Molecular Cell Biology *22*, 483-504.

Dictenberg, J. B., Swanger, S. A., Antar, L. N., Singer, R. H., & Bassell, G. J. (2008). A direct role for FMRP in activity-dependent dendritic mRNA transport links filopodial-spine morphogenesis to fragile X syndrome. *Developmental Cell*, *14*(6), 926–939.

Donlin-Asp, P.G., Polisseni, C., Klimek, R., Heckel, A., and Schuman, E.M. (2021). Differential regulation of local mRNA dynamics and translation following long-term potentiation and depression. Proceedings of the National Academy of Sciences of the United States of America *118*.

Doyle, M., and Kiebler, M.A. (2011). Mechanisms of dendritic mRNA transport and its role in synaptic tagging. The EMBO journal *30*, 3540-3552.

Dynes, J.L., and Steward, O. (2012). Arc mRNA docks precisely at the base of individual dendritic spines indicating the existence of a specialized microdomain for synapse-specific mRNA translation. The Journal of comparative neurology *520*, 3105-3119.

Falahati, H., Wu, Y., Feuerer, V., Simon, H.G., and De Camilli, P. (2022). Proximity proteomics of synaptopodin provides insight into the molecular composition of the spine apparatus of dendritic spines. Proc Natl Acad Sci U S A. *119*, e2203750119. doi: 10.1073/pnas.2203750119.

Fritzsche, R., Karra, D., Bennett, Keiryn L., Ang, Foong y., Heraud-Farlow, Jacki E., Tolino, M., Doyle, M., Bauer, Karl E., Thomas, S., Planyavsky, M.*, et al.* (2013). Interactome of Two

Diverse RNA Granules Links mRNA Localization to Translational Repression in Neurons. Cell reports *5*, 1749-1762.

Grant, S.G.N., and Fransén, E. (2020). The Synapse Diversity Dilemma: Molecular Heterogeneity Confounds Studies of Synapse Function. Frontiers in synaptic neuroscience *12*, 590403.

Hammer, J.A., 3rd, and Sellers, J.R. (2011). Walking to work: roles for class V myosins as cargo transporters. Nature reviews Molecular cell biology *13*, 13-26.

Hirokawa, N., and Takemura, R. (2004). Kinesin superfamily proteins and their various functions and dynamics. Experimental cell research *301*, 50-59.

Hirokawa, N., and Tanaka, Y. (2015). Kinesin superfamily proteins (KIFs): Various functions and their relevance for important phenomena in life and diseases. Experimental cell research *334*, 16-25.

Holland, E.D., Miller, H.L., Millette, M.M., Taylor, R.J., Drucker, G.L., and Dent, E.W. (2024). A methodology for specific disruption of microtubule polymerization into dendritic spines. Molecular biology of the cell *35*, mr3.

Holt, C.E., and Schuman, E.M. (2013). The central dogma decentralized: new perspectives on RNA function and local translation in neurons. Neuron *80*, 648-657.

Hu, X., Ballo, L., Pietila, L., Viesselmann, C., Ballweg, J., Lumbard, D., Stevenson, M., Merriam, E., and Dent, E.W. (2011). BDNF-induced increase of PSD-95 in dendritic spines requires dynamic microtubule invasions. The Journal of neuroscience : the official journal of the Society for Neuroscience *31*, 15597-15603.

Jaworski, J., Kapitein, L.C., Gouveia, S.M., Dortland, B.R., Wulf, P.S., Grigoriev, I., Camera, P., Spangler, S.A., Di Stefano, P., Demmers, J.*, et al.* (2009). Dynamic Microtubules Regulate Dendritic Spine Morphology and Synaptic Plasticity. Neuron *61*, 85-100.

Jedlicka, P., and Deller, T. (2017). Understanding the role of synaptopodin and the spine apparatus in Hebbian synaptic plasticity – New perspectives and the need for computational modeling. *Neurobiology of Learning and Memory*, *138*, 21–30.

Kaizuka, Takeshi, Taisei Hirouchi, Takeo Saneyoshi, et al. (2024). 'FAM81A Is a Postsynaptic Protein That Regulates the Condensation of Postsynaptic Proteins via Liquid–Liquid Phase Separation'. *PLOS Biology* 22 (3): e3002006

Kanai, Y., Dohmae, N., and Hirokawa, N. (2004). Kinesin Transports RNA: Isolation and Characterization of an RNA-Transporting Granule. Neuron *43*, 513-525.

Kao, D.I., Aldridge, G.M., Weiler, I.J., and Greenough, W.T. (2010). Altered mRNA transport, docking, and protein translation in neurons lacking fragile X mental retardation protein. Proceedings of the National Academy of Sciences of the United States of America *107*, 15601-15606.

Kiebler, M.A., and Bassell, G.J. (2006). Neuronal RNA granules: movers and makers. Neuron *51*, 685-

690.

Kim, Y., Jang, Y.N., Kim, J.Y., Kim, N., Noh, S., Kim, H., Queenan, B.N., Bellmore, R., Mun, J.Y., Park, H., *et al.* (2020). Microtubule-associated protein 2 mediates induction of long-term potentiation in hippocampal neurons. FASEB journal : official publication of the Federation of American Societies for Experimental Biology *34*, 6965-6983.

Kocsis, E., Trus, B.L., Steer, C.J., Bisher, M.E., and Steven, A.C. (1991). Image averaging of flexible fibrous macromolecules: The clathrin triskelion has an elastic proximal segment. Journal of Structural Biology *107*, 6-14.

Konietzny, A., Wegmann, S., and Mikhaylova, M. (2023). The endoplasmic reticulum puts a new spin on synaptic tagging. Trends in Neurosciences *46*, 32-44.

Lai, K.O., Zhao, Y., Ch'ng, T.H., and Martin, K.C. (2008). Importin-mediated retrograde transport of CREB2 from distal processes to the nucleus in neurons. Proceedings of the National Academy of Sciences of the United States of America *105*, 17175-17180.

Lin, L., Lo, L.H., Lyu, Q., and Lai, K.O. (2017). Determination of dendritic spine morphology by the striatin scaffold protein STRN4 through interaction with the phosphatase PP2A. The Journal of biological chemistry *292*, 9451-9464.

Lu, W., Man, H., Ju, W., Trimble, W.S., MacDonald, J.F., and Wang, Y.T. (2001). Activation of synaptic NMDA receptors induces membrane insertion of new AMPA receptors and LTP in cultured hippocampal neurons. Neuron *29*, 243-254.

Mikl, M., Vendra, G., and Kiebler, M.A. (2011). Independent localization of MAP2, CaMKIIα and β-actin RNAs in low copy numbers. EMBO reports *12*, 1077-1084.

Miryala, C. S. J., Holland, E. D., and Dent, E. W. (2022). Contributions of microtubule dynamics and transport to presynaptic and postsynaptic functions. *Molecular and Cellular Neuroscience*, *123*, 103787.

Mitsumori, K., Takei, Y., and Hirokawa, N. (2017). Components of RNA granules affect their localization and dynamics in neuronal dendrites. Molecular biology of the cell *28*, 1412-1417.

Nakahata, Y., & Yasuda, R. (2018). Plasticity of spine structure: Local signaling, translation and cytoskeletal reorganization. *Frontiers in Synaptic Neuroscience*, *10*(AUG), 391820.

Pierce, J.P., Mayer, T., and McCarthy, J.B. (2001). Evidence for a satellite secretory pathway in neuronal dendritic spines. Current biology : CB *11*, 351-355.

Pierce, J.P., van Leyen, K., and McCarthy, J.B. (2000). Translocation machinery for synthesis of integral membrane and secretory proteins in dendritic spines. Nature neuroscience *3*, 311-313.

Segal, M., Vlachos, A., and Korkotian, E. (2010). The spine apparatus, synaptopodin, and dendritic spine plasticity. The Neuroscientist : a review journal bringing neurobiology, neurology and

psychiatry *16*, 125-131.

Sheng, Z.H. (2014). Mitochondrial trafficking and anchoring in neurons: New insight and implications. The Journal of cell biology *204*, 1087-1098.

Steward, O., and Schuman, E.M. (2001). Protein synthesis at synaptic sites on dendrites. Annual review of neuroscience *24*, 299-325.

Swarnkar, S., Avchalumov, Y., Espadas, I., Grinman, E., Liu, X. an, Raveendra, B. L., Zucca, A., Mediouni, S., Sadhu, A., Valente, S., Page, D., Miller, K., & Puthanveettil, S. V. (2021). Molecular motor protein KIF5C mediates structural plasticity and long-term memory by constraining local translation. *Cell Reports*, *36*(2).

Swulius, M. T., Kubota, Y., Forest, A., & Waxham, M. N. (2010). Structure and Composition of the Postsynaptic Density during Development. *The Journal of Comparative Neurology*, *518*(20), 4243.

Tada, Tomoko, Alyson Simonetta, Matthew Batterton, Makoto Kinoshita, Dieter Edbauer, and Morgan Sheng. (2007). 'Role of Septin Cytoskeleton in Spine Morphogenesis and Dendrite Development in Neurons'. *Current Biology* 17 (20): 1752–58.

Tiruchinapalli, D.M., Oleynikov, Y., Kelic, S., Shenoy, S.M., Hartley, A., Stanton, P.K., Singer, R.H., and Bassell, G.J. (2003). Activity-dependent trafficking and dynamic localization of zipcode binding protein 1 and beta-actin mRNA in dendrites and spines of hippocampal neurons. The Journal of neuroscience : the official journal of the Society for Neuroscience *23*, 3251-3261.

Tübing, F., Vendra, G., Mikl, M., Macchi, P., Thomas, S., and Kiebler, M.A. (2010). Dendritically localized transcripts are sorted into distinct ribonucleoprotein particles that display fast directional motility along dendrites of hippocampal neurons. The Journal of neuroscience : the official journal of the Society for Neuroscience *30*, 4160-4170.

van Oostrum, M., and Schuman, E.M. (2025). Understanding the molecular diversity of synapses. Nature reviews Neuroscience *26*, 65-81.

Vlachos, A., Müller-Dahlhaus, F., Rosskopp, J., Lenz, M., Ziemann, U., and Deller, T. (2012). Repetitive magnetic stimulation induces functional and structural plasticity of excitatory postsynapses in mouse organotypic hippocampal slice cultures. The Journal of Neuroscience : The Official Journal of the Society for Neuroscience, *32*(48), 17514–17523.

Vlachos, A. (2012). Synaptopodin and the spine apparatus organelle-regulators of different forms of synaptic plasticity? Annals of anatomy *194*, 317-320.

Xie, Y., Vessey, J.P., Konecna, A., Dahm, R., Macchi, P., and Kiebler MA.(2007). The GTP-binding protein Septin 7 is critical for dendrite branching and dendritic-spine morphology. Current Biology. *17*, 1746-51. doi: 10.1016/j.cub.2007.08.042.

Yi, W., Li, J., Zhu, X., Wang, X., Fan, L., Sun, W., Liao, L., Zhang, J., Li, X., Ye, J., Chen, F., Taipale, J., Chan, K.M., Zhang, L., and Yan, J. (2020). CRISPR-assisted detection of RNA-protein interactions in living cells. Nature methods *17*, 685-688.

Yoon, Y.J., Wu, B., Buxbaum, A.R., Das, S., Tsai, A., English, B.P., Grimm, J.B., Lavis, L.D., and Singer, R.H. (2016). Glutamate-induced RNA localization and translation in neurons. Proceedings of the National Academy of Sciences of the United States of America *113*, E6877-e6886.

Zhao, J., Fok, A.H.K., Fan, R., Kwan, P.Y., Chan, H.L., Lo, L.H., Chan, Y.S., Yung, W.H., Huang, J., Lai, C.S.W., and Lai, K.O. (2020). Specific depletion of the motor protein KIF5B leads to deficits in dendritic transport, synaptic plasticity and memory. eLife *9*.

FIGURE LEGENDS

Figure 1. Spine base serves as a hotspot for mRNA localization

(A) Representative dual-color smFISH images of *Camk2a* (magenta) and *Actb* (red) mRNA puncta in different region of dendrites in rat hippocampal neurons. Neurons were transfected with GFP at 13 DIV, fixed at 21 DIV, and subjected to dual-color smFISH and immunostaining with anti-GFP antibody. Dendrites were outlined based on the GFP signals.

(B) Pie charts showing the proportion of the *Actb* and *Camk2a* mRNA puncta distributed to different dendritic compartments (the dendritic shaft, spine base, and spine head). The proportion of both mRNAs at the base is greater than that in the spine head. Results were pooled from two independent experiments; 19 neurons were imaged and 364-481 mRNA puncta from 40 primary basal dendrites were analyzed.

(C) Representative dual-color smFISH images showing co-localization of *Camk2a* (magenta) and *Actb* (red) mRNAs at the spine base.

(D) Quantification of mRNA co-localization, measured by M1 (percentage of *Actb* puncta overlapping with *Camk2a*) and M2 (percentage of *Camk2a* puncta overlapping with *Actb*). The two mRNAs exhibit preferential co-localization at the spine base. Each data point represents one neuron. Results were pooled from two independent experiments; 19 neurons were imaged and 364-481 mRNA puncta from 40 primary basal dendrites were quantified. Data are mean ± SEM; $^{**}p < 0.01$, $^{***}p < 0.001$, $^{****}p < 0.0001$; one-way ANOVA with Tukey's multiple comparisons test.

(E) Live imaging of MS2-*Actb* mRNA reporter (green) in dendrites of hippocampal neurons co-expressing Td-tomato (red). Neurons were transfected at 13 DIV and imaged at 19-21 DIV (one frame/10 s for 1,800 s). Left: trajectories of two *Actb* mRNA puncta (yellow and purple arrows) which were localized at the spine base and one *Actb* mRNA (green arrow) which was localized on the dendritic shaft were showed over time. Right: polar plots of heading and displacement for each mRNA.

(F) The mRNA at the spine base show less movement compared to that on the shaft. Quantification of total distance of movement (left) and maximum displacement (right) for *Actb* mRNAs initially located in the shaft or at the spine base. Results were pooled from two independent experiments; 31 neurons were imaged and 53-84 puncta from 35 dendrites were quantified. Data are mean ± SEM; $^{**}p < 0.01$, $^{****}p < 0.0001$; Student's t-test.

(G) Representative kymograph and dendrite image showing the docking of fast-moving *Actb* mRNAs (purple and blue arrows) at the base of two dendritic spines (white asterisks).

(H) Analysis of fast-moving *Actb* granules (velocity > 0.13 μm/s) to determine where they stop. Near half of the granules docked at the spine base. Results were pooled from two independent experiments; 31 neurons were imaged and 10-13 docking granules from 35 dendrites were quantified.

Figure 2. Targeting of mRNAs to dendritic spine in response to cLTP correlates with MAP2 entry

(A) Representative dendritic segments of rat hippocampal neurons transfected with GFP at 13 DIV and fixed at 21 DIV, with or without chemical LTP (cLTP) stimulation (200 μM glycine and 1 μM strychnine, 6 min), followed by returning to the original medium for 30 min and immunostaining with anti-GFP antibody.

(B) Cumulative frequency distribution of spine width for control and cLTP conditions. The spine width significantly increased after the synaptic stimulation. Results were pooled from three independent experiments; 1,757-2,045 protrusions from 32–37 neurons per condition were quantified. Data are mean ± SEM; ****$p < 0.0001$; Student's t-test.

(C) Co-presence between the same- (*Camk2a-Camk2a* or *Actb-Actb*) and different- (*Camk2a-Actb*) mRNA granules at the spine base under control and cLTP conditions. Rat hippocampal neurons were transfected with GFP at 13 DIV and were fixed at 21 DIV, with or without cLTP stimulation, subsequently returning to original medium for 30 min, followed by immunostaining with an anti-GFP antibody. After cLTP, different mRNAs relocate away from the co-localized spine bases. Each data point represents one neuron. Results were pooled from three independent experiments; 32-37 neurons per condition were imaged and 816-1,122 mRNA puncta from 96-111 dendrites per condition were quantified. Data are mean ± SEM; *$p < 0.05$, ****$p < 0.0001$; two-way ANOVA with Šídák's multiple comparisons test.

(D) The proportion of *Camk2a* and *Actb* mRNAs localized at the base and head of dendritic spines across different time points following cLTP. Neurons (transfected with GFP at 13 DIV) were subjected to cLTP at 21 DIV, fixed at the indicated time points, and processed for dual color smFISH combined with anti-GFP and anti-MAP2 immunostaining. The localization of mRNA puncta within primary basal dendrites was quantified and categorized as in the shaft, base, or head of dendritic spines. After stimulation, the proportion of *Actb* mRNA in spine heads increased significantly over time compared to *Camk2a*, whereas the proportion of *Camk2a* mRNA at spine bases showed a significant increase compared to *Actb*. Results were pooled from three independent experiments; 24 neurons per condition were imaged and 541–777 mRNA puncta from 72 primary basal dendrites per condition were

quantified. Data are mean ± SEM; **p < 0.01, ***p < 0.001; two-way ANOVA with Šídák's multiple comparisons test.

(E) Representative dendritic segments of rat hippocampal neurons from four experimental groups: control, cLTP, cLTP+APV, and APV. Neurons were transfected with GFP at 13 DIV and subjected to the respective treatments at 21 DIV (cLTP stimulation and/or APV application as indicated). After treatment, cells were returned to the original medium for 60 min and immune-stained with anti-GFP and anti-MAP2 antibodies. Yellow arrows indicate MAP2-positive spines; white arrows indicate MAP2-negative spines.

(F) Cumulative frequency distribution of the width of MAP2-positive (MAP2-pos) and -negative (MAP2-neg) spines. MAP2-pos spines showed larger spine width than MAP2-neg spines. Results were pooled from three independent experiments; 1,200-1,757 spines from 32 neurons per condition were quantified. Data are mean ± SEM; ****$p < 0.0001$; Student's t-test.

(G) Representative dendrites of neurons transfected with GFP at 13 DIV, subjected to cLTP at 21 DIV, returned to original medium for 30 min and followed by dual-color smFISH combined with anti-GFP and anti-MAP2 immunostaining. MAP2-positive spines showed increased mRNA accumulation at the head (pink arrow) or base (purple arrow).

(H) After cLTP, mRNAs preferentially accumulate at the head and base of MAP2-positive spines. Percentage of spines with mRNA localized at the head or base between MAP2-positive and MAP2-negative spines. Results were pooled from three independent experiments; A total of 32 neurons were imaged, with 2,208–2,441 mRNA puncta and 6,007–7,032 spines quantified. Data are mean ± SEM; ****$p < 0.0001$; Student's t-test.

(I) The proportion of MAP2-positive spines increases over time following cLTP induction. Rat hippocampal neurons were transfected with GFP at 13 DIV, subjected to cLTP stimulation at 21 DIV, and then returned to the original medium before fixation at the indicated time points (5, 15, 30, 45, 60 min). Results were pooled from three independent experiment; 951–1,837 spines from 24-26 neurons per condition were quantified. Data are mean ± SEM; ***$p < 0.001$, ****$p < 0.0001$; one-way ANOVA with Tukey's multiple comparisons test.

(J) The proportion of mRNAs localized at the base and head of dendritic spines increases over time following cLTP. Neurons (transfected with GFP at 13 DIV) were subjected to cLTP at 21 DIV, and then returned to the original medium before fixation at the indicated time points for dual-color smFISH combined with anti-GFP and anti-MAP2 immunostaining. The localization of mRNA puncta within

primary basal dendrites was quantified and categorized as in the dendritic shaft, base, or head of dendritic spines. Results were pooled from three independent experiments; 24-26 neurons per condition were imaged, and 1,455-1,914 mRNA puncta from 72 primary basal dendrites were quantified. Data are mean ± SEM; $*p < 0.05$, $**p < 0.01$, $***p < 0.001$; one-way ANOVA with Tukey's multiple comparisons test.

Figure 3. *Actb* and *Camk2a* mRNAs show heterogeneous and specific synaptic targeting after cLTP

(A) Representative dendritic segments of rat hippocampal neurons transfected with GFP at 13 DIV, subjected to cLTP at 21 DIV, then returned to original medium for 60 min, and processed for dual color smFISH combined with immunostaining for GFP and MAP2. Images showing *Actb* mRNA localized to a MAP2-negative spine (white arrow) while *Camk2a* mRNA localized to a MAP2-positive spine (yellow arrow) within the same dendrite.

(B) *Camk2a* exhibits stronger preference to localize at the head of MAP2-positive spines after cLTP. Results pooled from three independent experiments; 32 neurons per condition were imaged and 2,208-2,441 mRNA puncta, 6,007-7,032 spines per condition were quantified. $****p < 0.0001$; chi-square test.

(C) Higher proportion of SP-enriched spines contain ribosomal protein L4. Results are from three independent experiments; 3,197–3,598 spines from 28–30 neurons per condition were quantified.

(D) Upon the induction of cLTP, higher proportion of MAP2-positive spines are enriched with SP and contain L4 as compared to the MAP2-negative spines, which have similar proportion to the control neurons without cLTP. Results were pooled from three independent experiments; 894-1,997 spines from 27-29 neurons were quantified for each experimental condition.

(E) Representative primary basal dendrites of neurons transfected with BFP and GFP-SP at 13 DIV, subjected to cLTP at 21 DIV, and returned to original medium for 30 min followed by immunostaining with anti-BFP, anti-L4, and anti-MAP2 antibodies. Blue arrow: SP-enriched, L4-positive spine; red arrow: SP-enriched, L4-negative spine; green arrow: SP-normal, L4-positive spine; purple arrow: SP-normal, L4-negative spine.

(F) After cLTP, SP-enriched spines are more likely to localize *Actb* and *Camk2a* mRNAs at their base and head. Results were pooled from three independent experiments; 28-30 neurons were imaged for each condition and 1662-1974 mRNA puncta, 3197-3598 spines were quantified. Data are presented as mean ± SEM, $****p < 0.0001$, Student's *t*-test.

(G) Representative primary basal dendrites of neurons transfected with BFP and GFP-SP at 13 DIV, subjected to cLTP at 21 DIV, and processed for dual color smFISH with anti-BFP immunostaining. Image showing *Actb* mRNA localized to a normal spine (not SP-enriched, white arrow) and *Camk2a* mRNA localized to a SP-enriched spine (yellow arrow).

(H) *Camk2a* exhibits stronger preference to localize at the head of SP-enriched spines under control and cLTP conditions. Results from three independent experiments; 28–30 neurons per condition were imaged and 1,662–1,974 mRNA puncta; 3,197–3,598 spines per condition were quantified. ****$p < 0.0001$; chi-square test.

Figure 4. Localization of mRNAs to dendritic spines depends on microtubule entry

(A) Representative dendrites of neurons transfected with EB3-mApple and BFP at 13 DIV and subjected to cLTP stimulation at 21 DIV. Cells were fixed at the indicated time points (5, 15, 30, 45, 60 min) after cLTP and processed for anti-BFP and anti-MAP2 immunostaining. EB3-positive spine is indicated by orange arrow; EB3-negative spine is indicated by white arrow.

(B) Induced EB3 localization at dendritic spine head precedes MAP2 entry in response to cLTP induction. Rat hippocampal neurons were co-transfected with EB3-mApple and BFP at 13 DIV and subjected to cLTP stimulation at 21 DIV. Cells were fixed at indicated time points (5, 15, 30, 45, 60 min) after cLTP and processed for anti-BFP and anti-MAP2 immunostaining. The percentages of EB3-positive spines and MAP2-positive spines were quantified at each time point. Results were pooled from two independent experiments; 3,117–4,180 spines from 16 neurons per condition were quantified. Data are mean ± SEM; ****$p < 0.0001$; two-way ANOVA with Šídák's multiple comparisons test.

(C) EB3 granules are specifically enriched in MAP2-positive spines following cLTP. The proportion of EB3-positive spines was quantified in three categories: spines from unstimulated control neurons, and MAP2-positive or MAP2-negative spines from neurons after cLTP induction. EB3 showed a preferential association with MAP2-positive spines after potentiation. Results were pooled from two independent experiments; 884–4,180 spines from 16 neurons per condition were quantified. ****$p < 0.0001$; chi-square test.

(D) Representative dendrites of neurons transfected with LifeAct-Scramble or LifeAct-MTED and BFP at 13 DIV and subjected to cLTP stimulation at 21 DIV. Neurons were fixed at the indicated time points (5, 30, 60 min) after cLTP and processed for anti-BFP and anti-MAP2 immunostaining. EB3 and MAP2-positive spine are indicated by orange arrows; EB3-negative and MAP2-positive spine is indicated by blue arrow, EB3-negative and MAP2-negative spine is indicated by white arrow.

(E) The proportion of EB3-positive and MAP2-positive spines varies over time following cLTP induction. At 5 min, EB3 (a microtubule plus-end-binding protein) rapidly entered dendritic spines and subsequently declined, while MAP2 gradually increased over time. Specific disruption of microtubule polymerization into dendritic spines by LifeAct-MTED significantly reduced the percentage of spines containing EB3 or MAP2. Results were pooled from two independent experiments; 3,025–5,550 spines from 15-16 neurons per condition were quantified. Data are mean ± SEM; $**p < 0.01$, $****p < 0.0001$; two-way ANOVA with Šídák's multiple comparisons test.

(F) Selective disruption of microtubule polymerization into dendritic spines by LifeAct-MTED significantly impaired the localization of *Actb* and *Camk2a* mRNAs at the spine head and spine base, respectively after cLTP induction. Percentage of localization for *Camk2a* and *Actb* mRNA granules in the shaft, base, and head of dendritic spines of primary basal dendrites across different experimental conditions. Results were pooled from two independent experiments; 310-468 mRNA puncta from 15 neurons per condition were quantified. Data are mean ± SEM; $**p < 0.01$, $****p < 0.0001$; two-way ANOVA with Šídák's multiple comparisons test.

Figure 5. The kinesin motor protein KIF5A is specifically required for the transport of *Actb* and *Camk2a* mRNAs to dendritic spines after cLTP

(A) Representative apical dendrites of rat hippocampal neurons transfected with either GFP-scramble-shRNA or GFP-KIF5A-shRNA at 13 DIV, followed by dual-color smFISH at 21 DIV.

(B) KIF5A knockdown specifically reduces the density of *Camk2a* mRNA puncta in apical dendrites. Each data point represented one dendrite. Results were pooled from three independent experiments, 25-26 neurons per condition were quantified. Data are mean ± SEM, $****p < 0.0001$, Student's t-test.

(C) Knockdown of KIF5A reduced the level of *Camk2a*, but not that of *Actb* in the cell body, as indicated by the average intensity of the mRNA puncta. Each data point represented one neuron. Results were pooled from two independent experiments; 25-26 neurons per condition were quantified. Data are mean ± SEM, $*p < 0.05$, Student's t-test.

(D) Representative primary basal dendrites of rat hippocampal neurons transfected with GFP-scramble-shRNA or GFP-KIF5A-shRNA at 13 DIV, followed by cLTP stimulation at 21 DIV. Neurons were fixed for dual-color smFISH after 60 min to visualize *Camk2a* (magenta) and *Actb* (red).

(E) KIF5A but not the closely related homolog KIF5B is required for the dendritic spine localization of *Actb* and *Camk2a* mRNAs. Percentage of *Camk2a* (magenta) and *Actb* (red) localization in the

dendritic shaft, spine base and spine head of primary basal dendrites across the four experimental groups: scramble shRNA, KIF5A shRNA, KIF5A shRNA + KIF5A ir (rescue), and KIF5A shRNA + KIF5B ir (rescue). Results were pooled from one experiment; 128-304 mRNA puncta from 11-14 neurons per condition were quantified. Data are mean ± SEM; *$p < 0.05$, **$p < 0.01$, ****$p < 0.0001$; two-way ANOVA with Šídák's multiple comparisons test.

Figure 6. Dendritic RBPs identified to be in proximity to KIF5s by APEX-mediated labelling

(A) Schematic representation of the various KIF5-APEX2 constructs. C-terminal tail of mouse KIF5A (808-1027 aa), KIF5B (808-963 aa) and KIF5C (808-956 aa) were cloned into the C-terminal of APEX2, which contained a HA tag at the N-terminus.

(B) Schematic representation of the KIF5-APEX2 proximity labeling. APEX2 oxidizes biotin-phenols to biotin-phenoxyl radicals when H2O2 is added. These radicals subsequently biotinylate nearby proteins within a range of <20 nm. The biotinylated proteins are enriched using streptavidin beads and applied to subsequent analyses such as western blotting or mass spectrometry.

(C) Expression of various KIF5-APEX2 fusion proteins in cortical neuron. The HA-tagged KIF5-APEX2 plasmids were electroporated into primary cortical neurons at 0 DIV and were harvested at 14 DIV for western blot analysis (left panel) or immunofluorescence (right panel) using anti-HA antibody.

(D) Principal component analysis (PCA) plot of the KIF5-APEX2 mass spectrometry result. Each data point corresponded to one MS sample. The plot demonstrates a clear separation between four experimental groups.

(E) Venn diagram showing the overlap of the KIF5A, KIF5B, and KIF5C proximity-proteins. The numbers in the diagram represent proteins that are significantly enriched (adjusted p-value < 0.05, and fold change > 1.5 compared to the APEX2 control).

(F) Volcano plots showing the RBPs enriched in the proximity of KIF5A, KIF5B, and KIF5C. Significantly enriched proteins (adjusted p-value < 0.05 and fold change > 1.5) are colored in red. Several known RBPs are annotated, revealing their association with specific KIF5.

(G) Table summarizing the different dendritic RBPs enriched in the various KIF5 proximity proteomes. Previous studies demonstrating the dendritic localization of these RBPs were listed.

Figure 7. CARPID proximity labelling identified differential proteins enriched by *Actb* and *Camk2a* mRNAs

(A) Schematic representation of the CARPID plasmid constructs. The minidCas13X.1 were tagged with the biotin ligase BASU and GFP. Two gRNA sequences target two adjacent loci on the same

transcript were tagged with mCherry.

(B) Overview of the CARPID-MS workflow. Cortical neurons were electroporated with the two CARPID plasmids and were treated with 200 μM biotin at DIV16 (Biotin is denoted by red circles labeled 'B'). Interactors within the proximity of the bait mRNAs were labelled. After streptavidin pulldown, samples were subjected to LC-MS/MS.

(C) Correlation Matrix heat map shows the Pearson correlation coefficients (r) between *Camk2a*, *Actb*, and Ctrl gRNA. Cells are shaded according to the strength of relationships based on the Pearson correlation coefficients (r) ($p < 0.001$).

(D) Volcano plots illustrate the enrichment of proteins (up-regulated) that are associated with *Actb* mRNA (left, pink dots) and *Camk2a* mRNA (right, pink dots), as compared to the control gRNA (Fold Change $\geqslant 2$, P value < 0.05). RNA-binding proteins (RBPs) are labeled.

(E) Venn diagram shows the common and unique proteins between the *Camk2a* mRNA proximity (blue) and *Actb* mRNA proximity proteomes (orange). A total of 361 proteins were identified exclusively in the *Camk2a*-proximity proteome, and 304 proteins were identified exclusively in the *Actb*-proximity proteome. 160 proteins enriched by both mRNAs were identified.

(F) Comparison of the CARPID data with the PSD proteome datasets. The overlap between the two mRNA clusters determined by CARPID and the previously published PSD proteome database (purple) encompassing a total of 5,869 proteins (Takeshi et al., 2024) is shown.

(G) Gene Ontology (GO) terms enriched among the *Actb*- and *Camk2a* -proximity proteins as well as the overlapping proteins. Gene enrichment percentages are indicated by dot size. Dot color gradients represent Benjamini–Hochberg adjusted p values ($p < 0.05$).

Figure 8. Different subcellular colocalization between *Actb*/*Camk2a* mRNAs and the proteins identified by CARPID-MS in neuronal dendrites

(A) Table summarizing the number of proteins from the *Camk2a*- and *Actb*-proximity proteomes that are present in the GO terms related to postsynaptic functions. Only *Camk2a*-proximity proteins were identified in these GO terms.

(B) Representative dendritic segments of rat hippocampal neurons transfected with BFP at 13 DIV and subjected to cLTP at 21 DIV. After recovery in the original medium for 60 min, neurons were fixed for dual color smFISH and immunostaining against ZBP1 or Septin7. Enlarged views showing the co-localized RNA-protein at the base (Septin7-*Camk2a*) or head (ZBP1-*Actb*) of dendritic spines.

(C) Majority of Septin7-mRNA colocalization is detected at the base of dendritic spines. Pie charts showing the proportion of *Actb* and *Camk2a* mRNA puncta colocalized with ZBP1 or Septin7 at three

dendritic compartments: the shaft (yellow), spine base (red), and spine head (blue). Results were pooled from three independent experiments; 20-27 neurons were imaged and 298-455 mRNA puncta from 44-65 dendrites were analyzed.

SUPPLEMENTARY FIGURE LEGEND

Supplementary Figure 1

HEK 293T cells were transfected with GFP and Rattus norvegicus *Camk2a* mRNA CDS (NM_012920) or Rattus norvegicus *Actb* mRNA CDS (NM_031144). Dual color smFISH were performed using probes of distinct colors for *Camk2a* and *Actb* mRNAs to validate the specificity of the probes in labeling their respective mRNAs. Hybridization with the *Camk2a* mRNA sense probe and *Strn4* anti-sense probe served as negative control for the *in situ* hybridization.

Supplementary Figure 2

(A) Quantification of the density of individual spine types under control and cLTP conditions. Results were pooled from three independent experiments; 96-111 primary basal dendrites from 32-37 neurons were quantified for each condition. Data are mean ± SEM; $*p < 0.05$, Student's *t*-test.

(B) Cumulative frequency curve shows the width of the mushroom spines under control and cLTP conditions. Results were pooled from three independent experiments; 1,757-2,045 protrusions from 32–37 neurons per condition were quantified. Data are mean ± SEM; $****p < 0.0001$; Student's t-test.

(C) Representative dendrite showing an *Actb* mRNA puncta at the head of the dendritic spine (white arrow) in rat hippocampal neurons, which were transfected with the MS2-*Actb* mRNA reporter, MCP-GFP construct, and Td-tomato at DIV 13. Live cell imaging was conducted at DIV 21 with or without cLTP stimulation (one frame/10 s for 1,800 s).

(D) cLTP increased the occurrence of MS2-*Actb* reporter mRNA in the spine head. Pie chart was generated to display the proportion of puncta in each condition. All observable *Actb* puncta were classified into three categories (dendritic shaft, spine base or spine head) based on their location at the first frame of imaging,. Results were pooled from three independent experiments; 19-23 neurons were imaged and 116-141 mRNA puncta from 57-68 dendrites were quantified for each experimental condition.

(E) Quantification of the total movements and maximum displacement of each *Actb* mRNA under the control and cLTP conditions. Results were pooled from three independent experiments; 19-23 neurons were imaged for each experimental condition and 116-141 mRNA puncta from 57-68 dendrites were quantified for each experimental condition. Data are presented as mean ± SEM, $*p < 0.05$, $***p < 0.001$, $****p < 0.0001$, two-way ANOVA with Šídák's multiple comparisons test.

(F) Quantification of total movements per minute and maximum displacement of each *Actb* mRNA after cLTP. Results were pooled from three independent experiments; 19 neurons were imaged and 141 mRNA puncta from 68 dendrites were quantified. Data are presented as mean ± SEM, $*p < 0.05$, $**p < 0.01$, one-way ANOVA with Tukey's multiple comparisons test.

Supplementary Figure 3

(A) The proportion of neurons containing MAP2-positive spines increases following glycine-induced cLTP in a time-dependent manner. Neurons were subjected to glycine stimulation (200 μM) for 3 or 6 minutes, fixed, and stained for MAP2. The percentage of neurons with MAP2-positive spines was quantified under each condition. Each data point represents the value from one independent experiment of cultured neurons. n = 10 experiment (control), n = 7 experiments (control, 3 min glycine), n = 5 experiments (control, 6 min glycine); 10–20 neurons were analysed per condition in each experiment. Data are mean ± SEM; $****p < 0.0001$; one-way ANOVA with Tukey's multiple comparisons test.

(B) MAP2 entry to dendritic spines after cLTP depends on NMDA receptors. Neurons were transfected with GFP at 13 DIV and subjected to the respective treatments at 21 DIV (cLTP stimulation and/or APV application as indicated). After treatment, cells were recovered in original medium for 60 min before staining with anti-GFP and anti-MAP2 antibodies. 7-8 dendrites from 4-5 neurons per condition were quantified. Data are mean ± SEM; $****p < 0.0001$; one-way ANOVA with Tukey's multiple comparisons test.

(C) Rat hippocampal neurons were transfected with GFP at 13 DIV and fixed at 21 DIV. Following cLTP stimulation, all dendritic spines in neurons were classified to determine the relative proportion of MAP2-positive and MAP2-negative spines. Results were pooled from three independent experiments; 1,200-1,757 spines from 32 neurons per condition were quantified. Data are mean ± SEM; Student's t-test.

(D) The density of *Camk2a* and *Actb* mRNA puncta is not changed after cLTP. Rat hippocampal neurons were transfected with GFP at DIV 13, fixed at DIV 21 with or without cLTP stimulation and performed smFISH and immunolabeled with anti-GFP antibody. Each data point represented an individual value for each dendrite of neuron. Results were pooled from three independent experiments; 96-111 primary basal dendrites from 32-37 neurons were quantified for each condition. Data are mean ± SEM; Student's *t*-test.

Supplementary Figure 4

(A) Representative dendritic segments of rat hippocampal neurons transfected with BFP and GFP-SP at DIV 13, fixed at DIV 21 after cLTP stimulation, and immunolabeled with anti-BFP antibody. Yellow arrow indicates SP-enriched spine, white arrow indicates normal spine without SP enrichment.

(B) Representative dendritic segments of rat hippocampal neurons transfected with BFP and GFP-SP at DIV 13, fixed at DIV 21 after cLTP stimulation, and performed dual color smFISH and immunolabeled with anti-BFP antibody. SP-enriched spines attracted more mRNAs within their head or base. Pink arrow indicates SP-enriched spines with mRNA at the head; purple arrow indicates SP-enriched spines with mRNA at the base.

Supplementary Figure 5

(A) Effect of disrupting microtubule entry to spine on spine density. Neurons were transfected with LifeAct-Scramble or LifeAct-MTED along with BFP at 13 DIV, subjected to cLTP stimulation at 21 DIV. Neurons were fixed at the indicated time points (5, 30, and 60 minutes) after cLTP and processed for anti-BFP and anti-MAP2 immunostaining. No significant differences in spine density were observed between LifeAct-scramble control and LifeAct-MTED except 30 mins after cLTP. Results were pooled from two independent experiments; 3,025–5,550 spines from 15-16 neurons per condition were quantified. Data are mean ± SEM; $*p < 0.05$, $***p < 0.001$; one-way ANOVA with Tukey's multiple comparisons test.

(B) Following cLTP, EB3 density significantly increased in neurons transfected with LifeAct-scramble control. Specific disruption of microtubule polymerization into dendritic spines by LifeAct-MTED abolished the increased EB3 density. Results were pooled from two independent experiments; 40-50 dendrites from 15-16 neurons per condition were quantified. Data are mean ± SEM; $*p < 0.05$, $**p < 0.01$, $***p < 0.001$; $****p < 0.0001$; one-way ANOVA with Tukey's multiple comparisons test.

(C) Effect of disrupting microtubule entry to spine on EB3 and MAP2 localization in the spine heads. Following cLTP, the proportion of MAP2-positive spines among the EB3-positive spines and the proportion of EB3-positive spines among the MAP2-positive spines were quantified. Results were pooled from two independent experiments; 3,025–5,550 spines from 15-16 neurons per condition were quantified. Data are mean ± SEM; $*p < 0.05$, $**p < 0.01$; two-way ANOVA with Šídák's multiple comparisons test.

(D) Effect of KIF5A depletion on the proximo-distal distribution of *Camk2a* and *Actb* mRNA along apical dendrites. Knockdown of KIF5A altered the distribution of *Camk2a* mRNA, but not that of *Actb* mRNA. Results were pooled from three independent experiments; 25-26 neurons per condition were

quantified. Data are mean ± SEM; ****$p < 0.0001$; two-way ANOVA with Šídák's multiple comparisons test.

(E) Rat hippocampal neurons were transfected with GFP-scramble-shRNA or GFP-KIF5A-shRNA at 13 DIV and subjected to cLTP stimulation at 21 DIV. After recovery for 60 min, neurons were processed for dual-color smFISH of *Camk2a* (magenta) and *Actb* (red) mRNA puncta. Cumulative frequency distribution of spine width for different conditions. After stimulation, the spine width was significantly increased in neurons expressing scramble shRNA control or KIF5A-shRNA, indicating kncodown of KIF5A does not affect the neuronal response to cLTP. Results are pooled from two independent experiments; 798-1589 spines from 16-17 neurons per condition were quantified. Data are presented as mean ± SEM; one-way ANOVA with Tukey's multiple comparisons test.

(F) Spine density was quantified for the different conditions, and no significant differences were observed between conditions. Results are pooled from two independent experiments; 798-1589 spines from 16-17 neurons per condition were quantified. Data are presented as mean ± SEM; one-way ANOVA with Tukey's multiple comparisons test.

(G) The density of *Camk2a* and *Actb* mRNA puncta within the same dendrite was compared between each experimental condition. Each dot represented an individual value for each dendrite of neuron. Results were pooled from two independent experiments; 304-546 mRNA puncta from 16-17 neurons per condition were quantified. Data are mean ± SEM; *$p < 0.05$, **$p < 0.01$; one-way ANOVA with Tukey's multiple comparisons test.

Supplementary Figure 6

(A) Representative confocal images of co-electroporation of CARPID plasmids. Images showed cortical neurons co-expressing BASU-minidCas13X.1 plasmid with either *Actb* gRNA (top panel), *Camk2a* gRNA (middle panel), or Control gRNA (bottom panel). Their estimated co-electroporation efficiencies were similar (51%, 39%, and 34% respectively). Neurons were stained with antibodies against MAP2, GFP and mCherry. Scale bar, 100 μm.

(B) Principal Component Analysis (PCA) shows distinct clusters corresponding to *Actb* (red), *Camk2a* (green), and control (Ctrl) gRNA (blue); whereas individual replicates of each particular gRNAs cluster together, indicating high consistencies among the biological triplicates

Figure 1

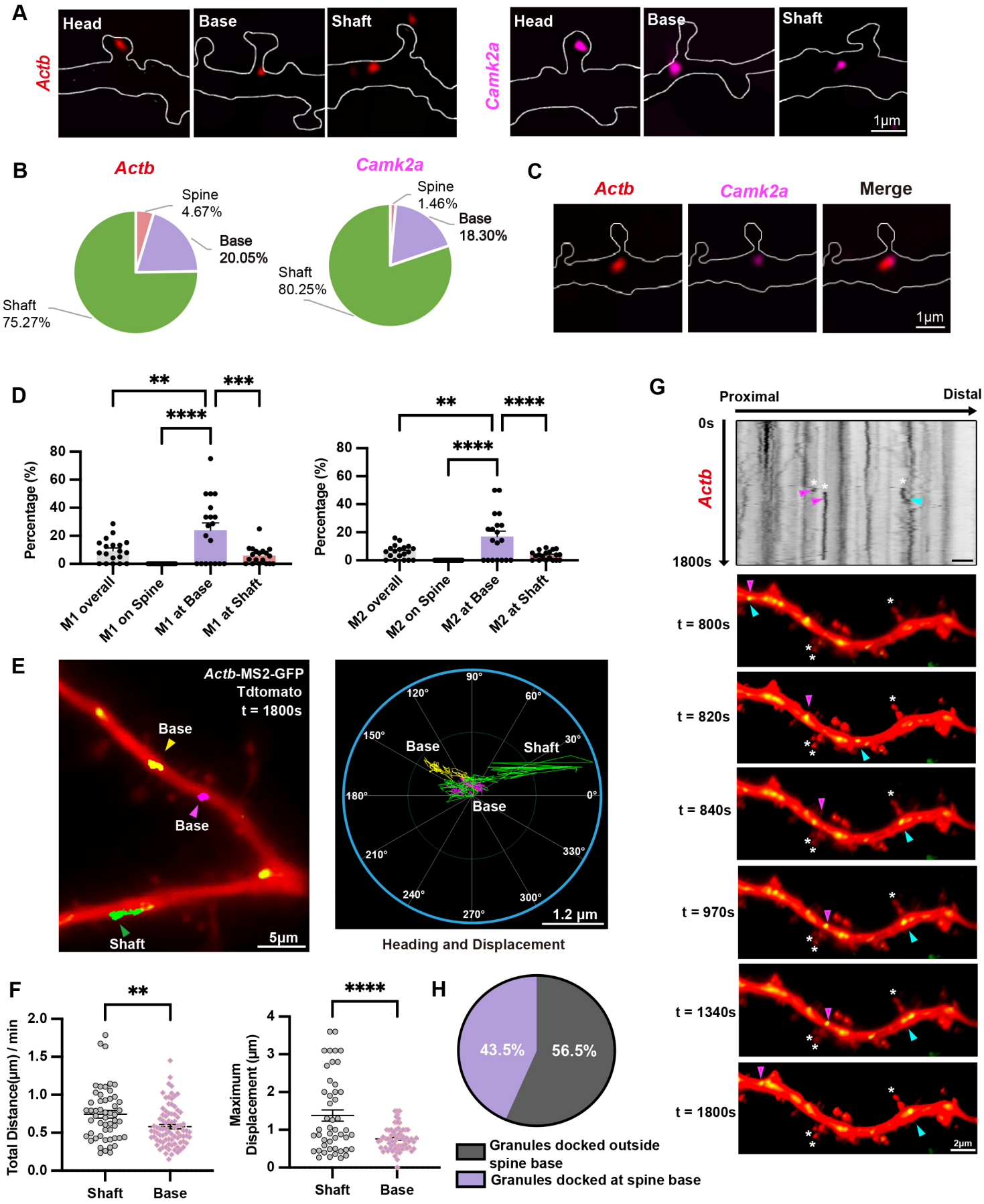
A
Actb
Head
Base
Shaft
Camk2a
Head
Base
Shaft
1μm
B
Actb
Spine
4.67%
Base
20.05%
Shaft
75.27%
Camk2a
Spine
1.46%
Base
18.30%
Shaft
80.25%
C
Actb
Camk2a
Merge
1μm
D
Percentage (%)
M1 overall
M1 on Spine
M1 at Base
M1 at Shaft
M2 overall
M2 on Spine
M2 at Base
M2 at Shaft
E
Actb-MS2-GFP
Tdtomato
t = 1800s
Base
Base
Shaft
5μm
Base
Shaft
Base
1.2 μm
Heading and Displacement
F
Total Distance(μm) / min
Maximum Displacement (μm)
Shaft
Base
H
43.5%
56.5%
Granules docked outside spine base
Granules docked at spine base
G
Proximal
Distal
0s
Actb
1800s
t = 800s
t = 820s
t = 840s
t = 970s
t = 1340s
t = 1800s
2μm

Figure 2

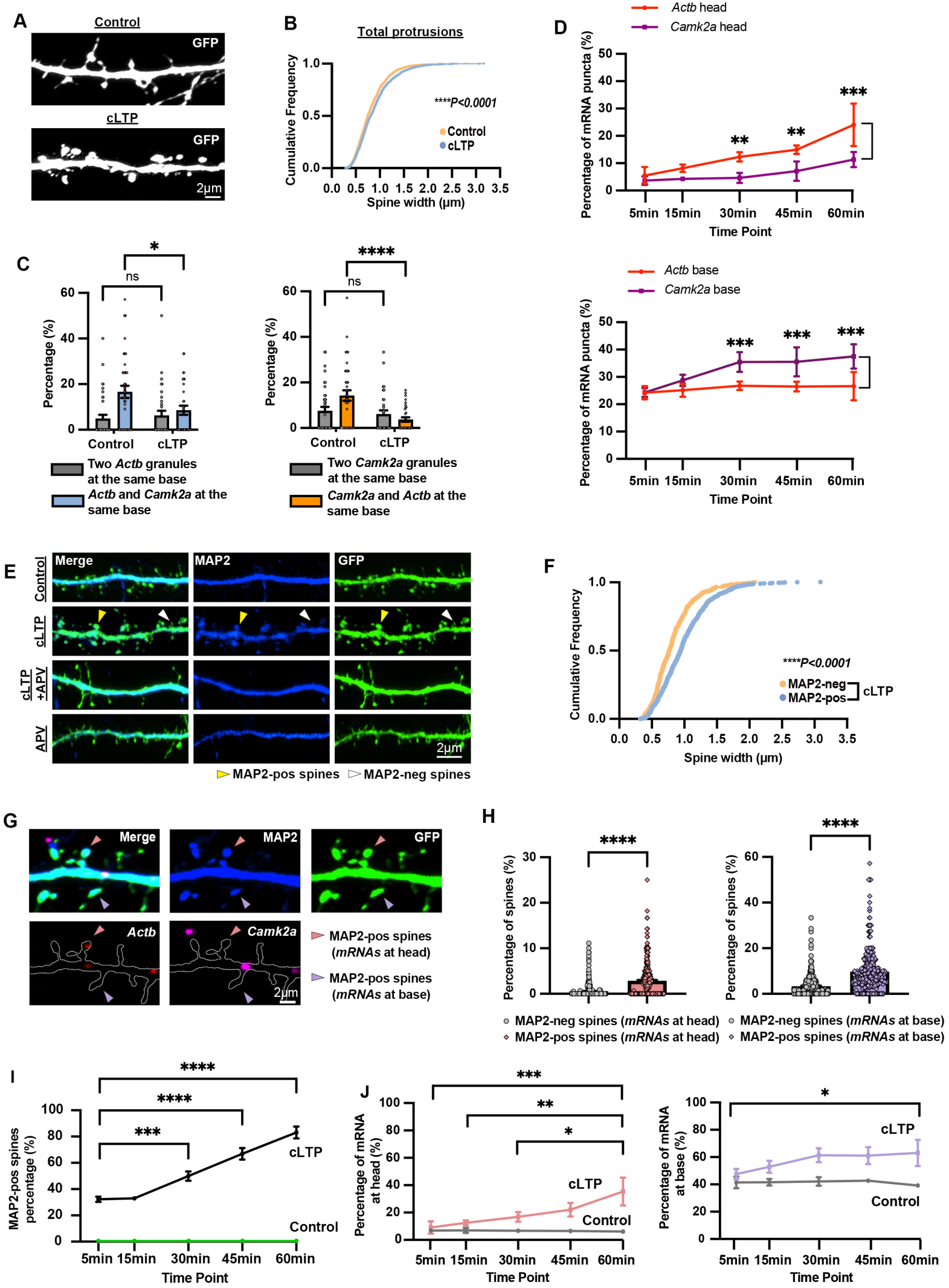
A
Control
GFP
cLTP
GFP
2μm
B
Total protrusions
Cumulative Frequency
1.0
0.5
0.0
****P<0.0001
Control
cLTP
0.0 0.5 1.0 1.5 2.0 2.5 3.0 3.5
Spine width (μm)
D
Actb head
Camk2a head
Percentage of mRNA puncta (%)
50 40 30 20 10 0
**
**
***
5min 15min 30min 45min 60min
Time Point
Actb base
Camk2a base
Percentage of mRNA puncta (%)
50 40 30 20 10 0
***
***
***
5min 15min 30min 45min 60min
Time Point
C
*
ns
Percentage (%)
60 40 20 0
Control cLTP
Two Actb granules at the same base
Actb and Camk2a at the same base
****
ns
Percentage (%)
60 40 20 0
Control cLTP
Two Camk2a granules at the same base
Camk2a and Actb at the same base
E
Control
cLTP
cLTP +APV
APV
Merge
MAP2
GFP
2μm
MAP2-pos spines
MAP2-neg spines
F
Cumulative Frequency
1.0
0.5
0.0
****P<0.0001
MAP2-neg
MAP2-pos
cLTP
0.0 0.5 1.0 1.5 2.0 2.5 3.0 3.5
Spine width (μm)
G
Merge
MAP2
GFP
Actb
Camk2a
2μm
MAP2-pos spines (mRNAs at head)
MAP2-pos spines (mRNAs at base)
H
****
Percentage of spines (%)
30 20 10 0
****
Percentage of spines (%)
60 40 20 0
MAP2-neg spines (mRNAs at head)
MAP2-pos spines (mRNAs at head)
MAP2-neg spines (mRNAs at base)
MAP2-pos spines (mRNAs at base)
I
****
****
***
MAP2-pos spines percentage (%)
100 80 60 40 20 0
cLTP
Control
5min 15min 30min 45min 60min
Time Point
J
***
**
*
Percentage of mRNA at head (%)
100 80 60 40 20 0
cLTP
Control
5min 15min 30min 45min 60min
Time Point
*
Percentage of mRNA at base (%)
100 80 60 40 20 0
cLTP
Control
5min 15min 30min 45min 60min
Time Point

Figure 3

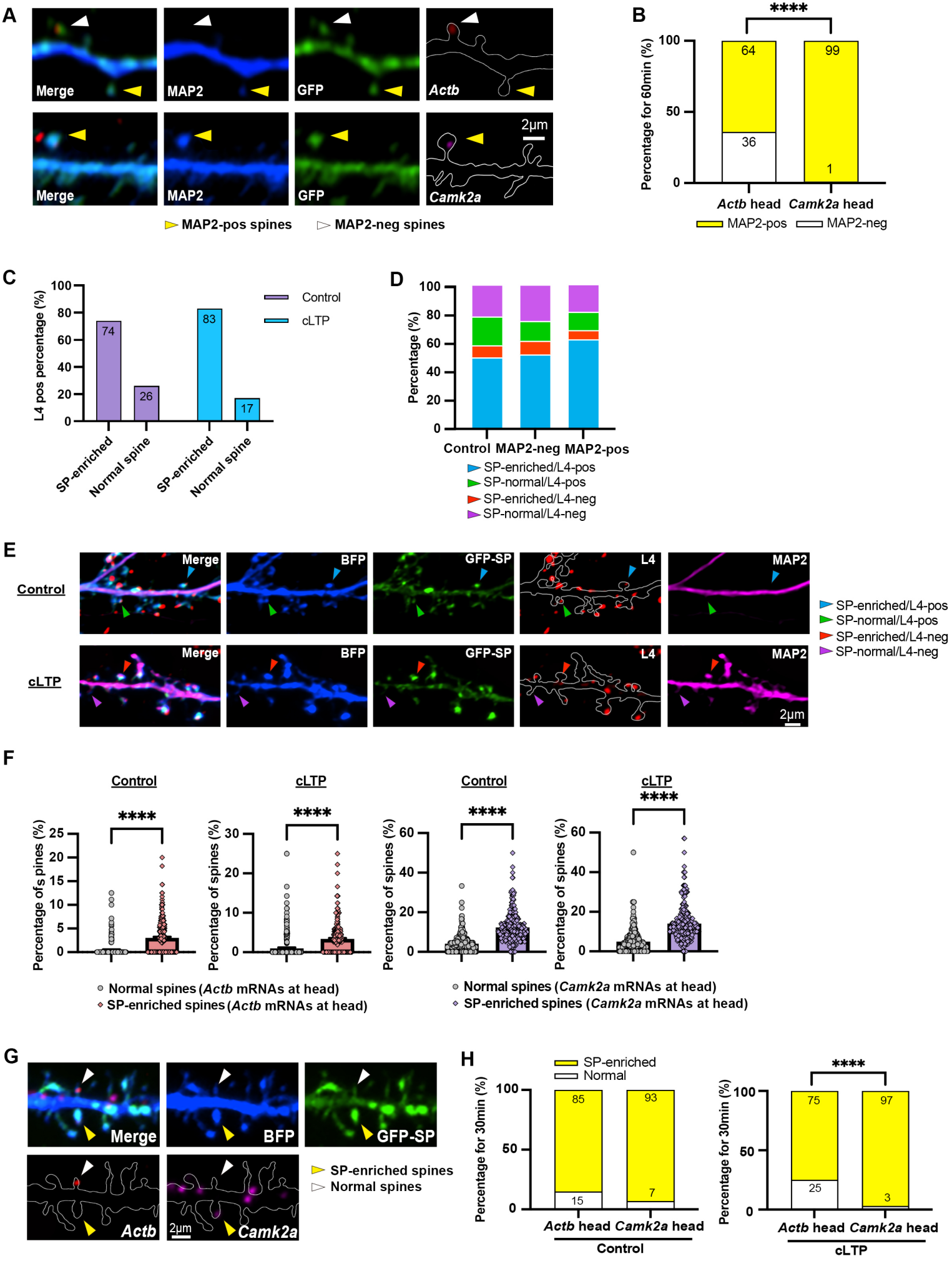
A
Merge
MAP2
GFP
Actb
Merge
MAP2
GFP
Camk2a
2μm
MAP2-pos spines
MAP2-neg spines
B
****
Percentage for 60min (%)
100
50
0
64
99
36
1
Actb head
Camk2a head
MAP2-pos
MAP2-neg
C
L4 pos percentage (%)
100
80
60
40
20
0
74
26
83
17
Control
cLTP
SP-enriched
Normal spine
SP-enriched
Normal spine
D
Percentage (%)
100
80
60
40
20
0
Control
MAP2-neg
MAP2-pos
SP-enriched/L4-pos
SP-normal/L4-pos
SP-enriched/L4-neg
SP-normal/L4-neg
E
Control
cLTP
Merge
BFP
GFP-SP
L4
MAP2
2μm
SP-enriched/L4-pos
SP-normal/L4-pos
SP-enriched/L4-neg
SP-normal/L4-neg
F
Control
cLTP
Control
cLTP
****
Percentage of s pines (%)
Percentage of spines (%)
Normal spines (Actb mRNAs at head)
SP-enriched spines (Actb mRNAs at head)
Normal spines (Camk2a mRNAs at head)
SP-enriched spines (Camk2a mRNAs at head)
G
Merge
BFP
GFP-SP
Actb
2μm
Camk2a
SP-enriched spines
Normal spines
H
SP-enriched
Normal
Percentage for 30min (%)
85
93
15
7
75
97
25
3
Actb head
Camk2a head
Control
cLTP

Figure 4

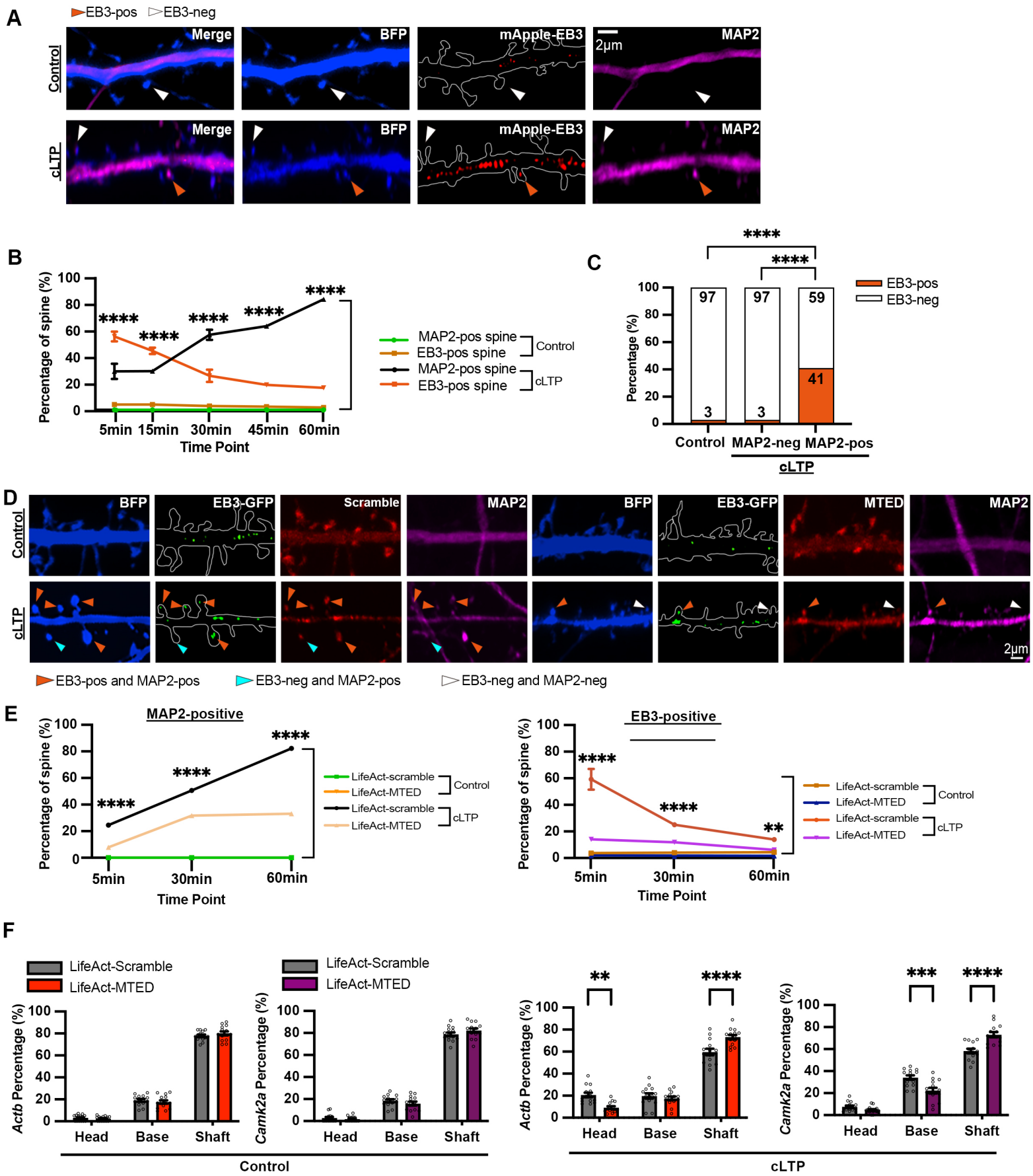
A
EB3-pos
EB3-neg
Control
cLTP
Merge
BFP
mApple-EB3
MAP2
2μm
B
Percentage of spine (%)
Time Point
5min
15min
30min
45min
60min
MAP2-pos spine
EB3-pos spine
Control
cLTP
C
Percentage (%)
97
3
97
3
59
41
Control
MAP2-neg
MAP2-pos
cLTP
D
EB3-GFP
Scramble
MTED
2μm
EB3-pos and MAP2-pos
EB3-neg and MAP2-pos
EB3-neg and MAP2-neg
E
MAP2-positive
EB3-positive
LifeAct-scramble
LifeAct-MTED
F
LifeAct-Scramble
LifeAct-MTED
Actb Percentage (%)
Camk2a Percentage (%)
Head
Base
Shaft
Control
cLTP

Figure 5

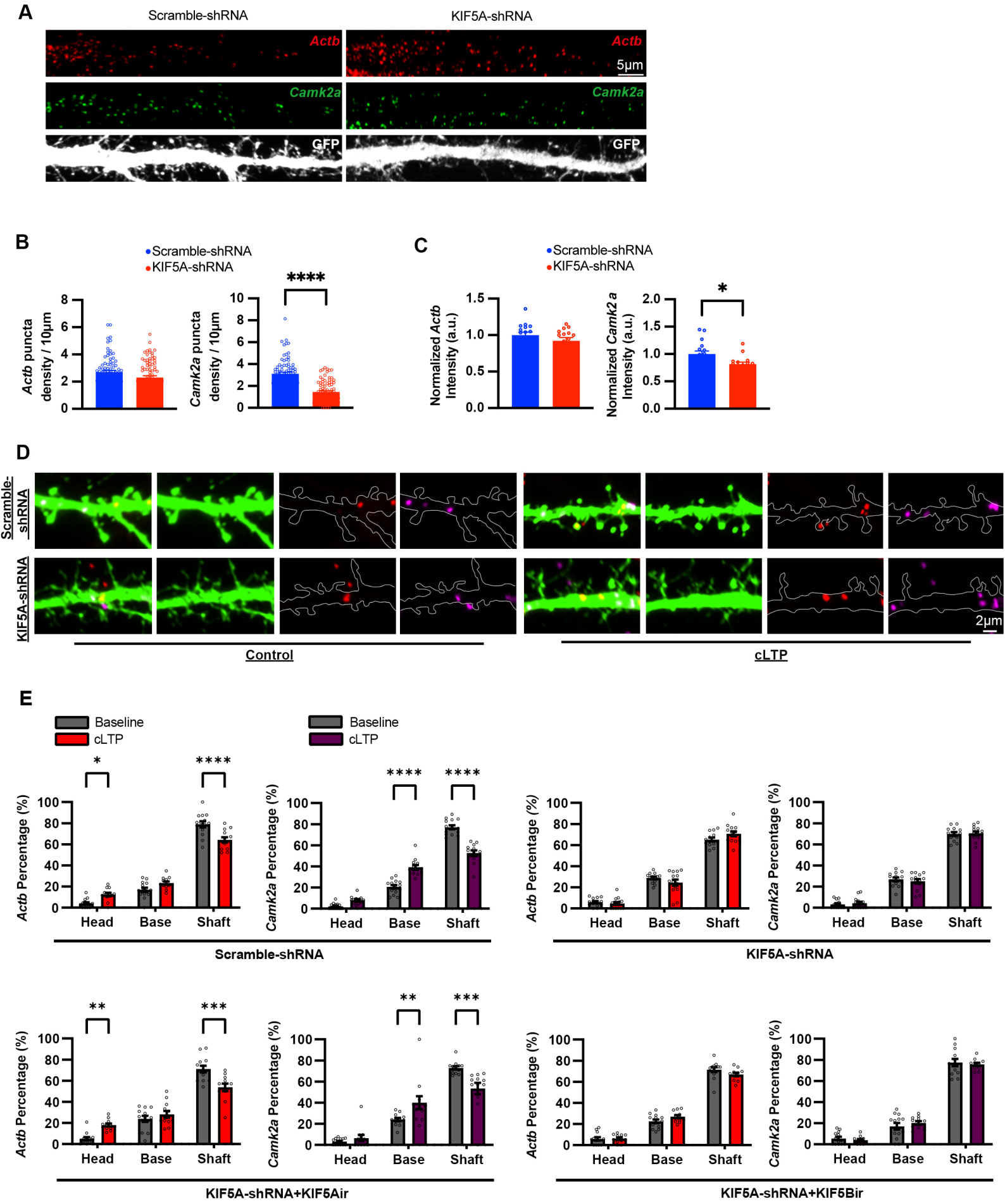
A
Scramble-shRNA
KIF5A-shRNA
Actb
Camk2a
GFP
5μm
B
Scramble-shRNA
KIF5A-shRNA
Actb puncta density / 10μm
Camk2a puncta density / 10μm
****
C
Scramble-shRNA
KIF5A-shRNA
Normalized Actb Intensity (a.u.)
Normalized Camk2a Intensity (a.u.)
*
D
Scramble-shRNA
KIF5A-shRNA
2μm
Control
cLTP
E
Baseline
cLTP
Actb Percentage (%)
Camk2a Percentage (%)
Head
Base
Shaft
Scramble-shRNA
KIF5A-shRNA
KIF5A-shRNA+KIF5Air
KIF5A-shRNA+KIF5Bir

Figure 6

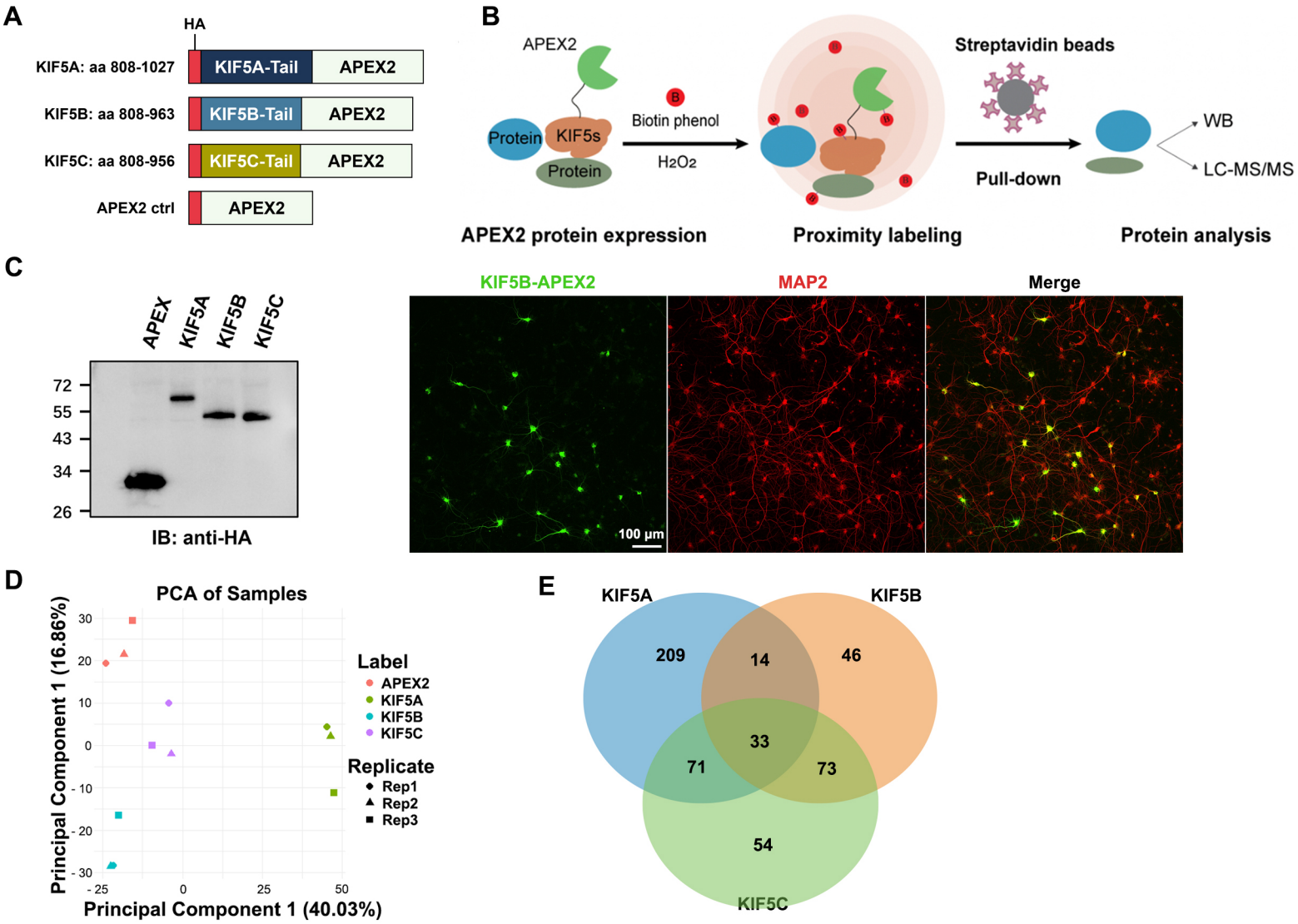

G

Cluster	Gene	Presented in PSD dataset (Kaizuka et al., 2024)	Reference
5A|5B|5C	KHDRBS1 (Sam68)	Yes	Klein et al., 2013, Fredj et al., 2004
5A|5C	EIF4A3	Yes	Giorgi et al., 2007
5B|5C	CAPRIN1	Yes	Fatimy et al., 2012
5B|5C	YBX1	Yes	Mei et al., 2025
5A	FMR1	Yes	Fok et al., 2024
5A	UPF2	Yes	Notaras et al., 2019
5A	DHX9	Yes	Yang et al., 2024
5A	UPF3B	No	Notaras et al., 2019
5B	JAKMIP1	Yes	Couve et al., 2004
5B	CPEB4	Yes	Huang et al., 2006
5C	HNRNPK	Yes	Leal et al., 2017
5C	HNRNPA3	Yes	Ma et al., 2002

Figure 7

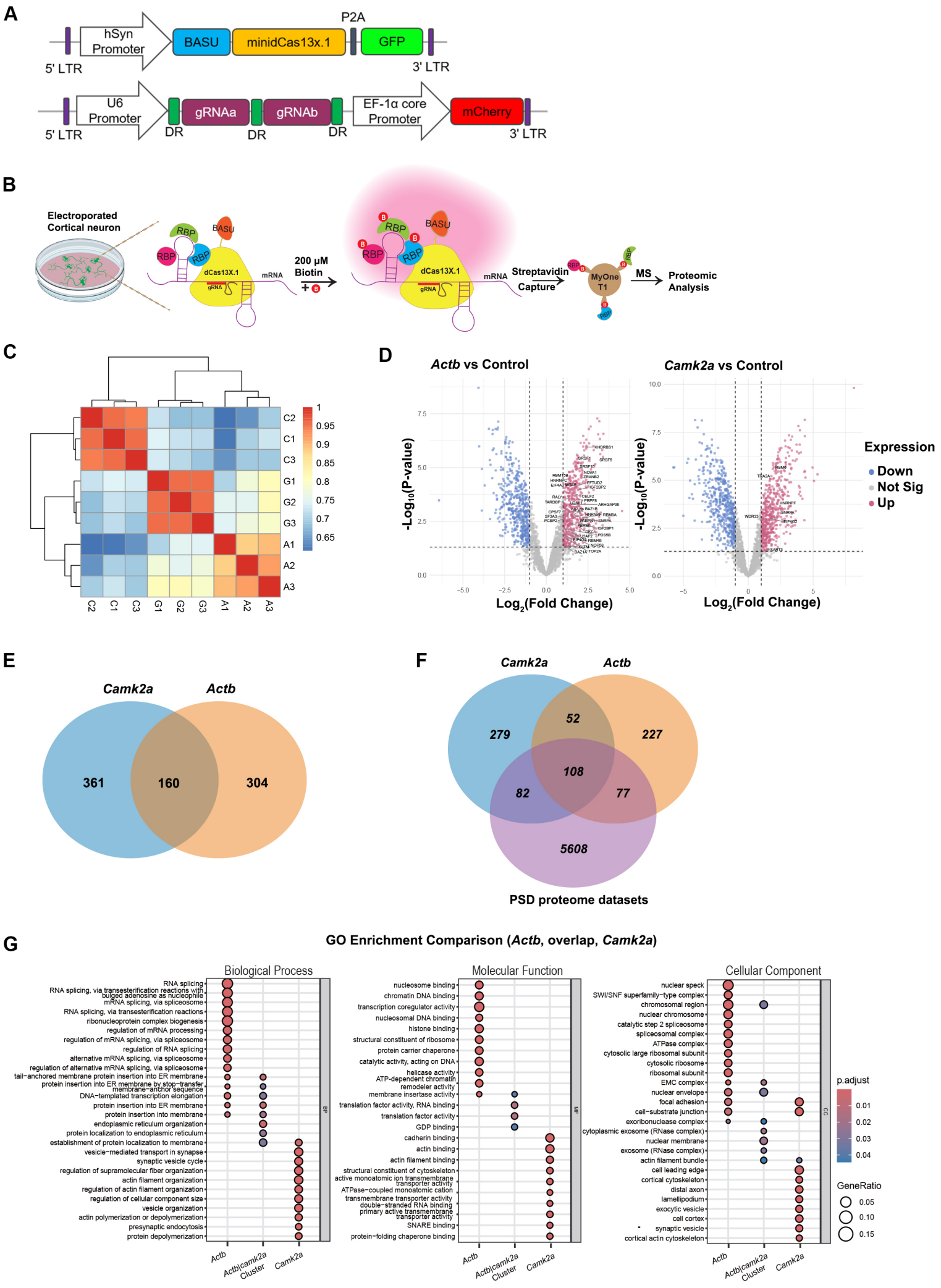
A
hSyn Promoter
BASU
minidCas13x.1
P2A
GFP
5' LTR
3' LTR
U6 Promoter
gRNAa
gRNAb
DR
EF-1α core Promoter
mCherry
B
Electroporated Cortical neuron
RBP
BASU
dCas13X.1
gRNA
mRNA
200 μM Biotin
Streptavidin Capture
MyOne T1
MS
Proteomic Analysis
C
D
Actb vs Control
Camk2a vs Control
-Log10(P-value)
Log2(Fold Change)
Expression
Down
Not Sig
Up
E
Camk2a
Actb
361
160
304
F
279
52
227
108
82
77
5608
PSD proteome datasets
G
GO Enrichment Comparison (Actb, overlap, Camk2a)
Biological Process
Molecular Function
Cellular Component
Actb
Actb|camk2a Cluster
Camk2a
p.adjust
GeneRatio

Figure 8

A

Go Term	Ontology	*Camk2a* cluster count	*Actb* cluster Count
Postsynapse organization	BP	18	0
Modification of postsynaptic actin cytoskeleton	BP	8	0
Regulation of modification of postsynaptic structure	BP	4	0
Regulation of modification of synaptic structure	BP	4	0
Postsynaptic density	CC	16	0
Postsynaptic specialization	CC	17	0
Postsynaptic membrane	CC	14	0
Postsynaptic specialization membrane	CC	9	0
Structural constituent of postsynapse	MF	5	0
Structural constituent of postsynaptic actin cytoskeleton	MF	3	0

B

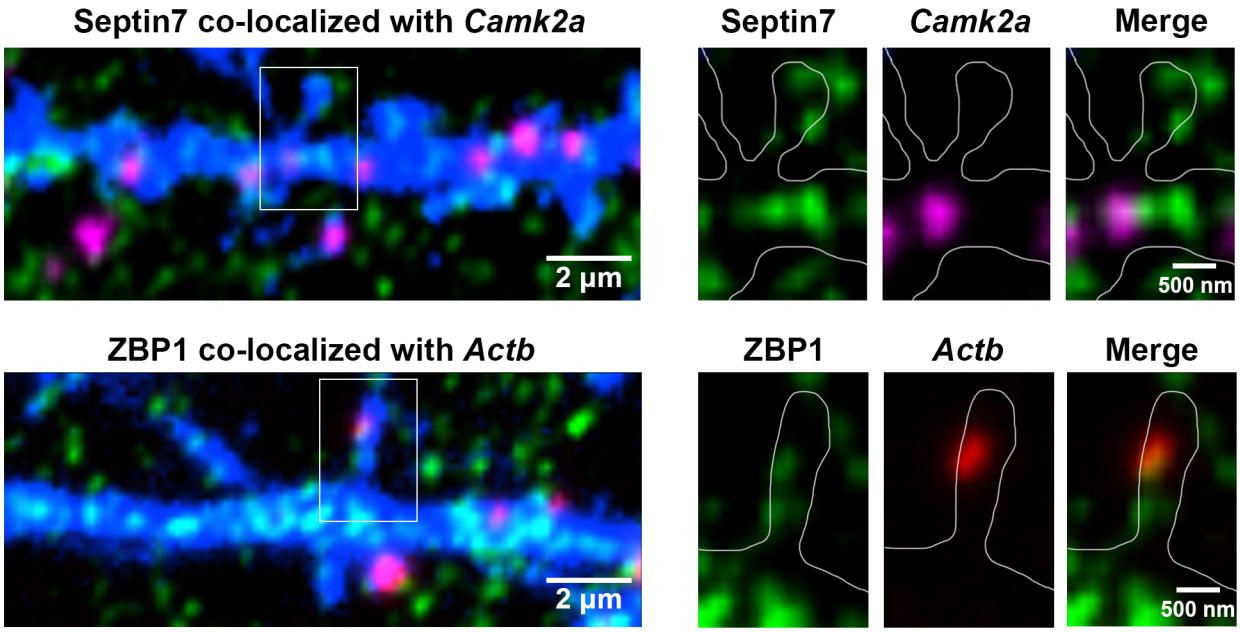

C

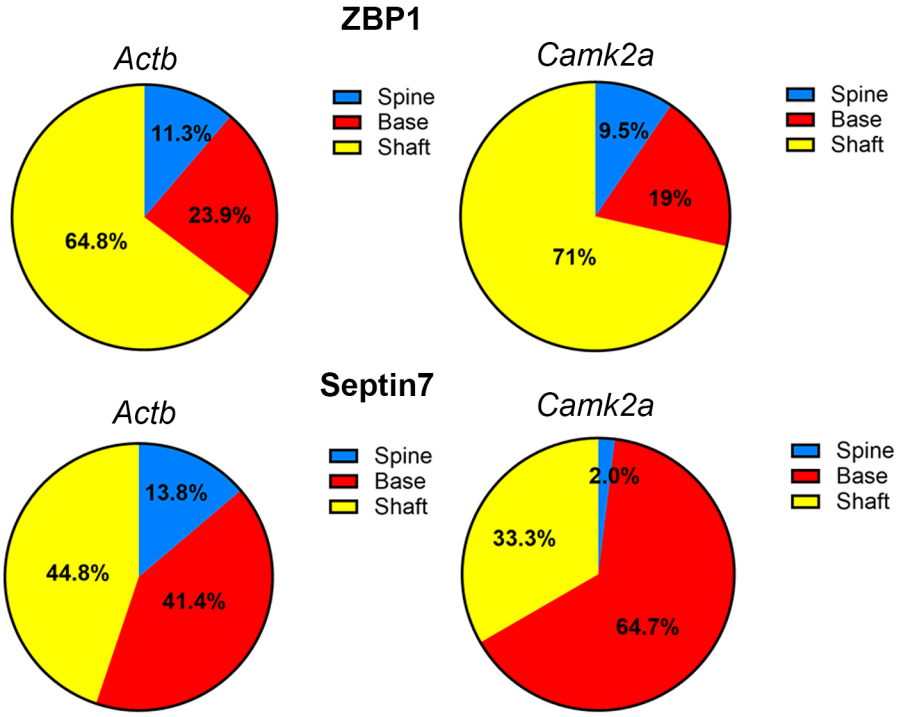

Supplementary Figure 1

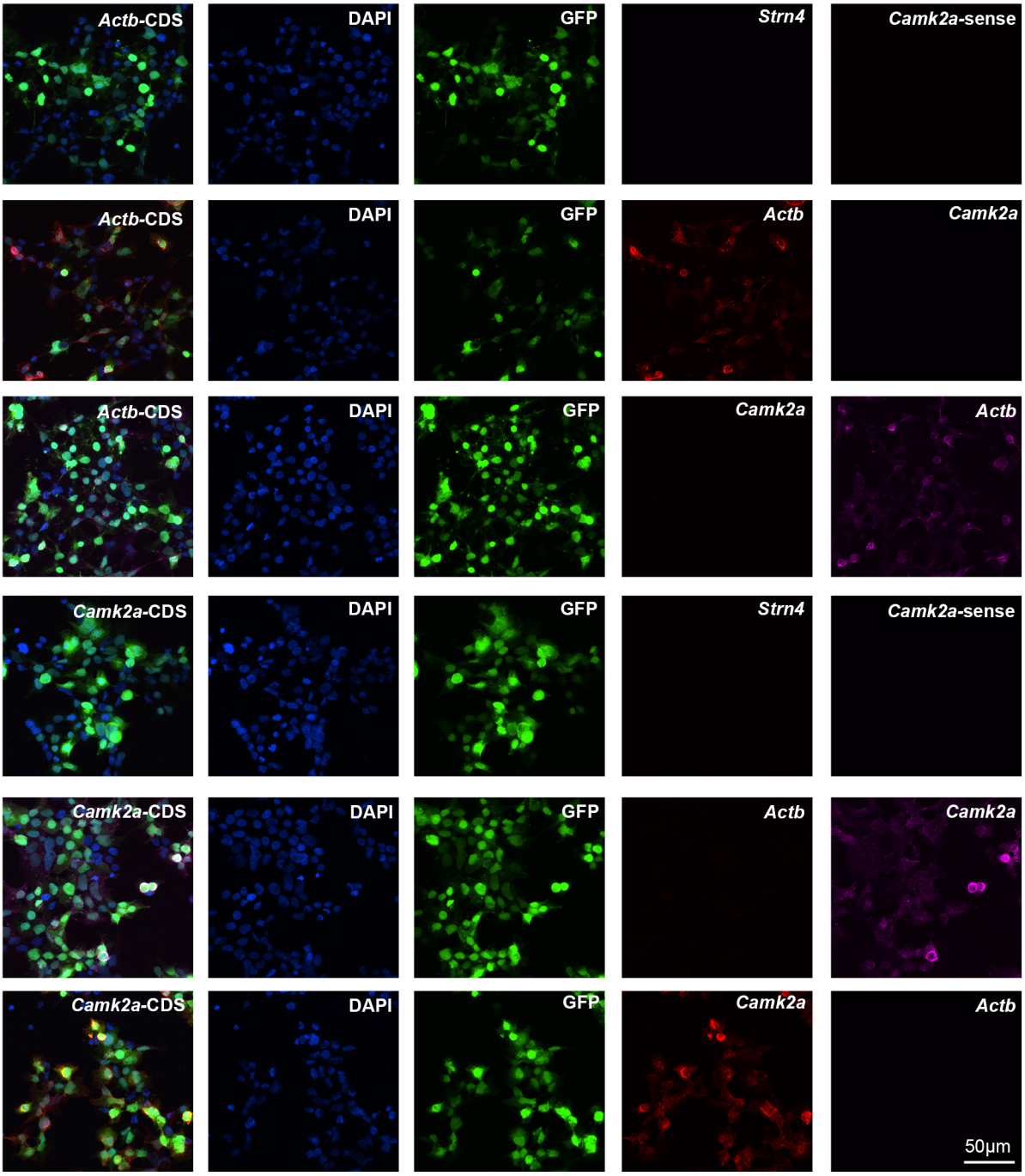

Supplementary Figure 2

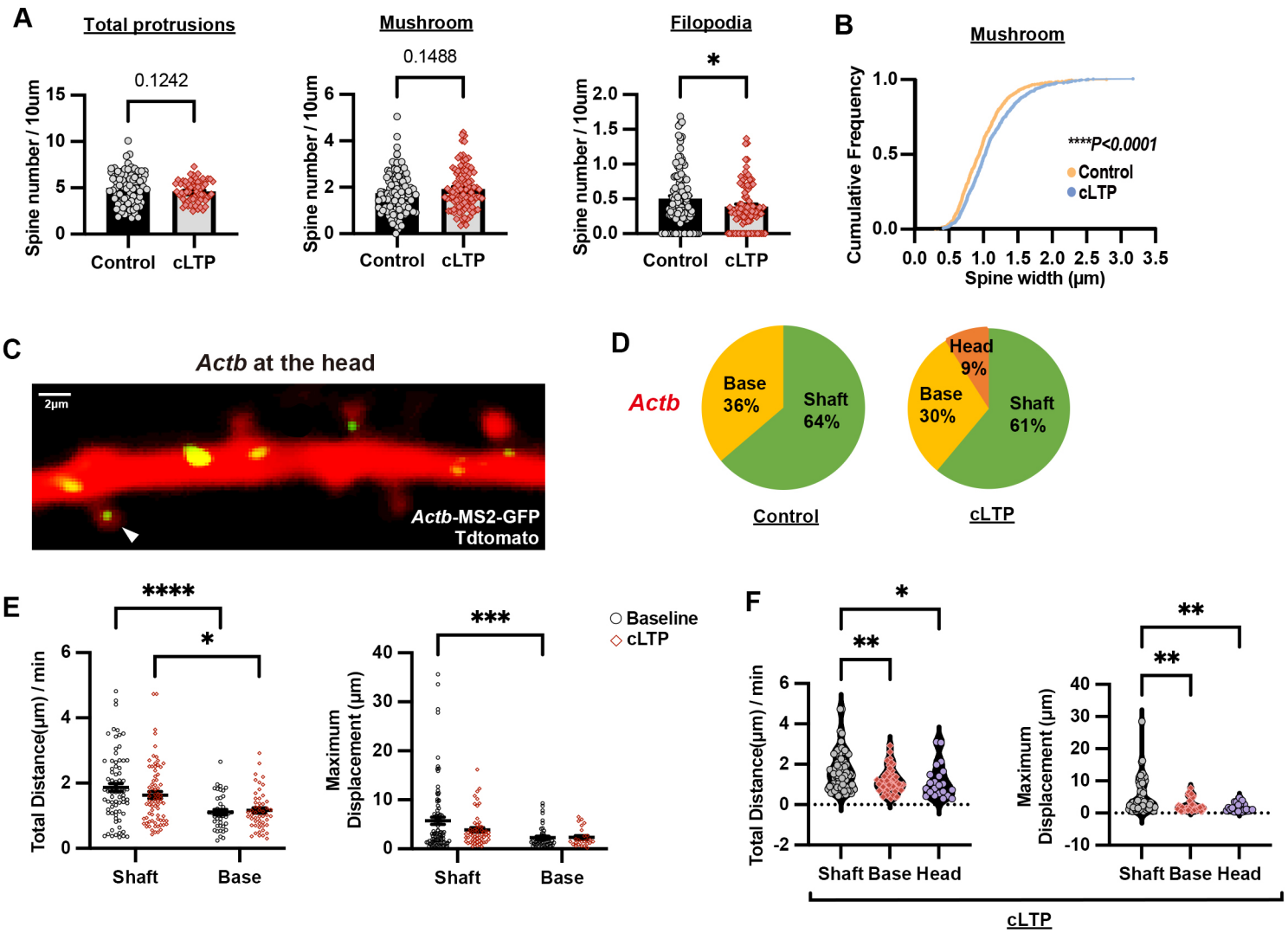

Supplementary Figure 3

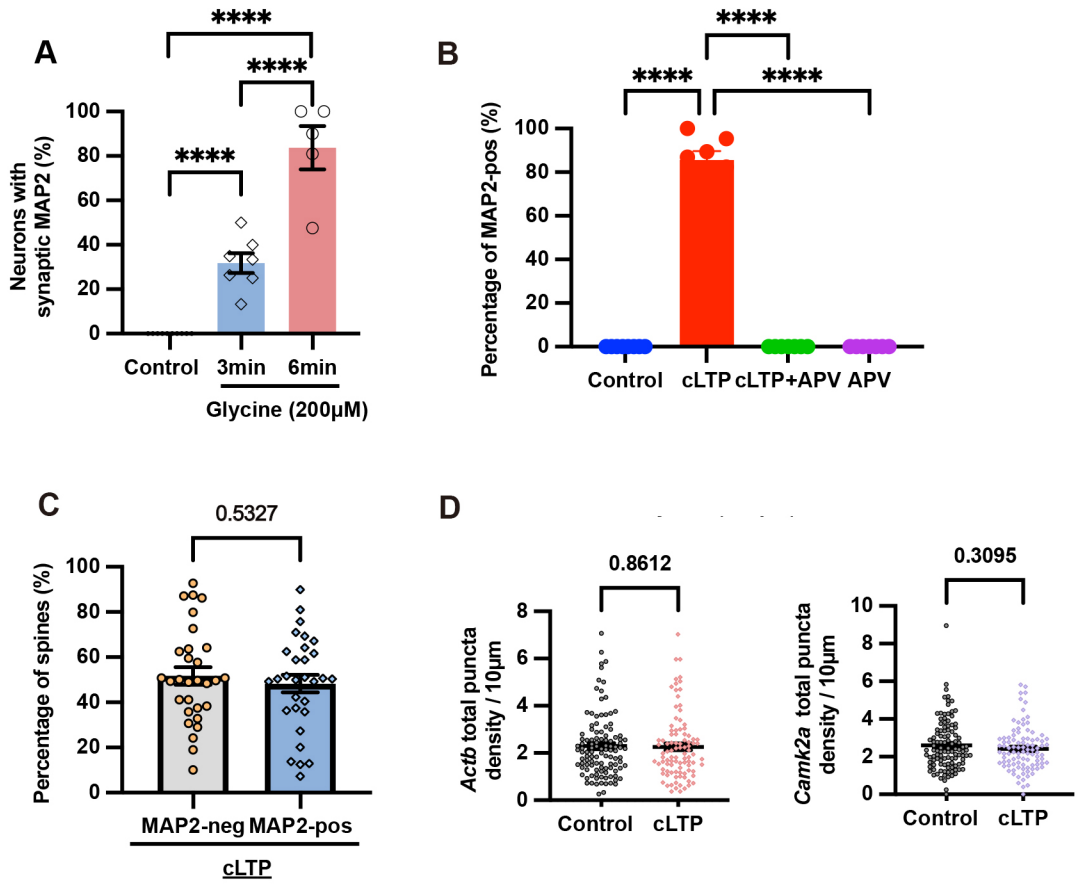

Supplementary Figure 4

A

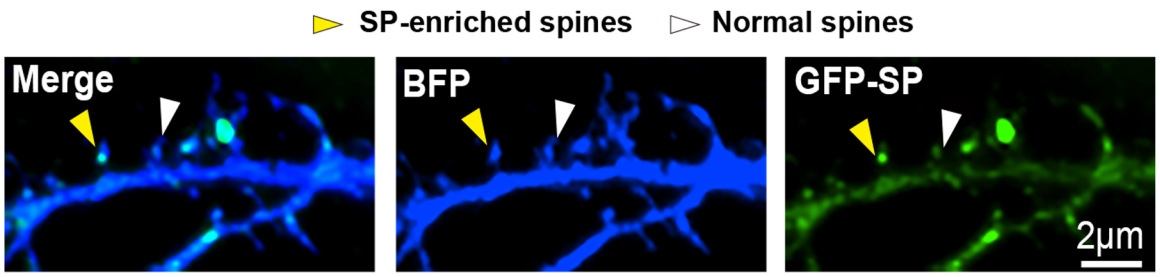

B

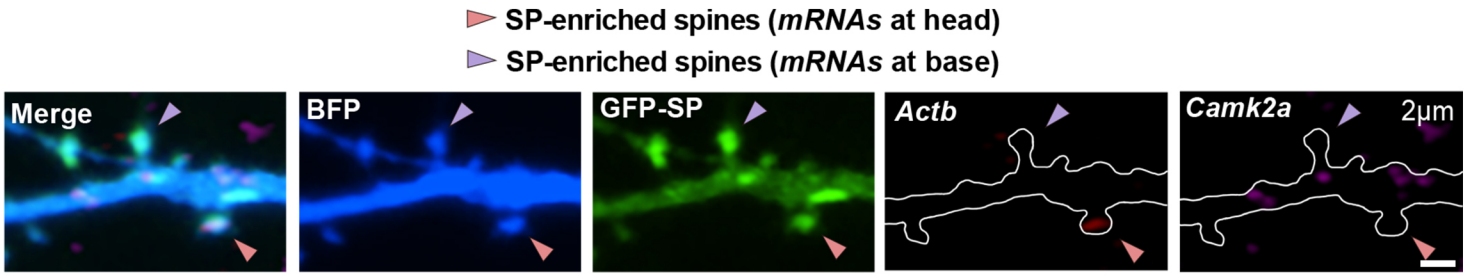

Supplementary Figure 5

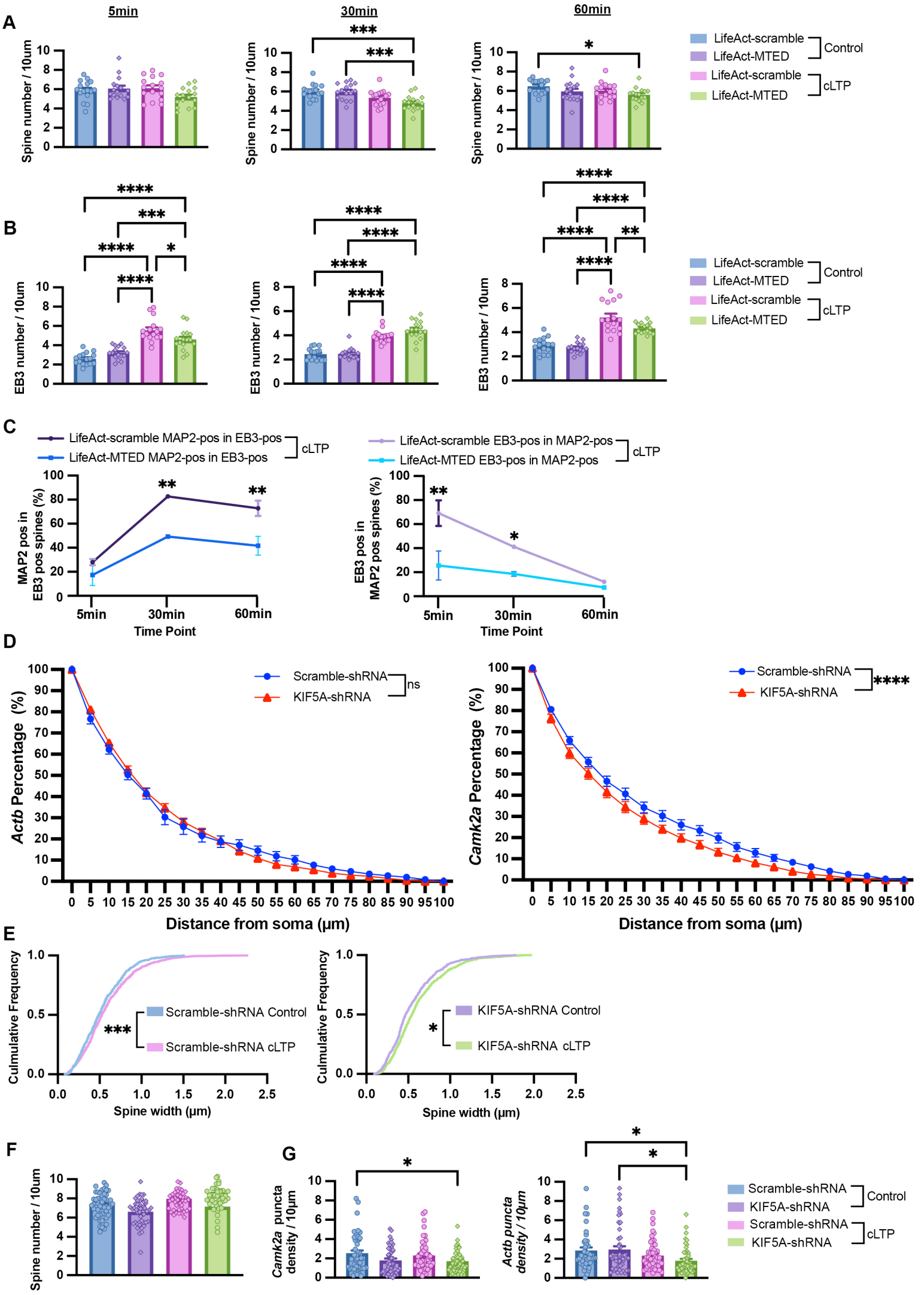

Supplementary Figure 6

A

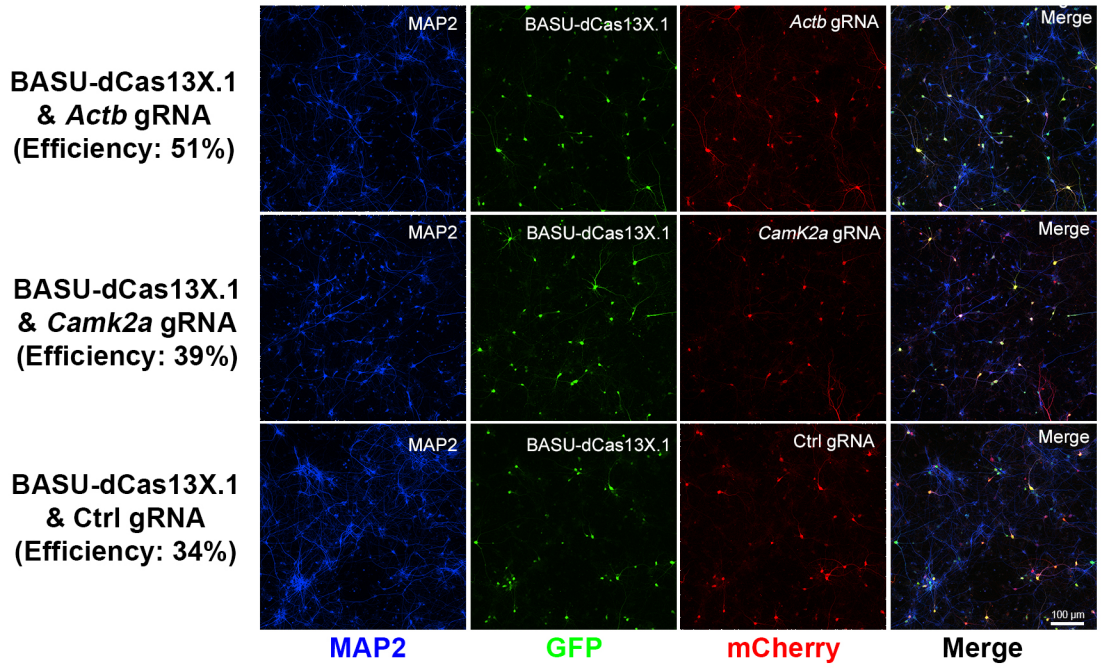
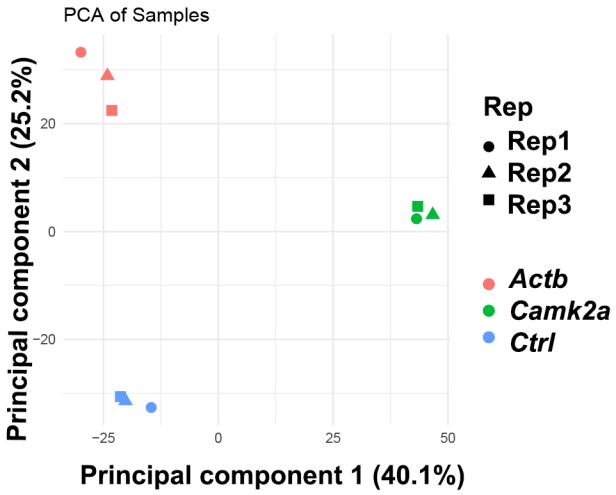
B